

Contents lists available at ScienceDirect

Journal of Computational Physics

journal homepage: www.elsevier.com/locate/jcp



Jacobian-free Newton-Krylov method for the simulation of non-thermal plasma discharges with high-order time integration and physics-based preconditioning



Alfredo Duarte Gomez*, Nicholas Deak, Fabrizio Bisetti

Department of Aerospace Engineering and Engineering Mechanics, The University of Texas at Austin, Austin, TX 78712, United States of America

ARTICLE INFO

Article history:
Received 22 August 2022
Received in revised form 4 January 2023
Accepted 8 February 2023
Available online 14 February 2023

Keywords:
Streamer discharge
Backward differentiation formulas
Jacobian-free Newton-Krylov
Physics-based preconditioning
PETSc
Non-thermal plasma

ABSTRACT

A preconditioning framework for the numerical simulation of non-thermal streamer discharges is developed using the Jacobian-free Newton-Krylov (JFNK) method. A reduced plasma fluid model is considered, consisting of electrons, one positive ion, one negative ion, and the electrostatic potential. The plasma kinetics model includes ionization, electron-ion recombination, electron attachment, electron detachment, and ion-ion recombination. The governing equations are made dimensionless, discretized in space with finite differences, and integrated in time with a fully implicit method based on high-order backward differentiation formulas. The preconditioning framework is based on a linearized form of the governing equations and physics-based operator splitting. The efficiency of the preconditioning strategy is assessed through two test cases: streamer propagation between parallel plates and an axisymmetric pin-to-pin discharge. The fully implicit approach overcomes traditional restrictions in the time step size due to processes such as electron drift, electron diffusion, and dielectric relaxation. Excellent performance is observed through relevant statistics of the JFNK solver, although the number of linear iterations increases for the pin-to-pin discharge when nonlinear numerical boundary conditions are imposed at the electrodes. Performance studies show scalability with $\mathcal{O}(100\text{-}1000)$ processors for $\mathcal{O}(10\,\mathrm{M})$ unknowns with ample room for optimization.

© 2023 Elsevier Inc. All rights reserved.

1. Introduction

Streamer discharges consist of a self-supported ionization wave that propagates from regions of high electric field towards those locations where the electric field is below breakdown. This phenomenon occurs in a variety of gaseous mixtures and it has become an object of interest in low temperature plasma technology. Examples of its applications include ignition of reactive mixtures [1], water treatment and reduction of pollutant emissions [2,3], fuel reforming [4], and medical devices [5].

Streamers generated during Nanosecond Pulsed Discharges (NPD) have received significant attention due to desirable features of energy deposition by high reduced electric fields $\mathcal{O}(100\text{-}1000\text{ Td})$ over short periods of time $\mathcal{O}(1\text{-}20\text{ ns})$. Additionally, low-temperature NPDs can be designed to limit heating at the electrodes, which improves the lifetime of the electrode and reduces energy loss. The numerical simulation of streamers has significant challenges. The smallest length

E-mail address: aduarteg@utexas.edu (A. Duarte Gomez).

^{*} Corresponding author.

scales of streamers are $\mathcal{O}(1~\mu m)$, which is very small compared to the size of the electrode gap $\mathcal{O}(1-100~mm)$. Simulations are further complicated by the separation of time scales between streamer phenomena and voltage pulse (0-50 ns) and bulk fluid transport (0-100 ms) as well as the tight coupling between plasma species through chemical kinetic processes. The development of robust, efficient, and stable numerical methods is key to predictive simulations of streamer discharges over multiple pulses.

Early streamer simulations relied on explicit time integration schemes [6,7]. However, ionization time scales associated with number densities $\mathcal{O}(10^{18}\text{-}10^{21}~\text{m}^{-3})$ at reduced electric fields $\mathcal{O}(100\text{-}1000~\text{Td})$ limit the time step size below tenths of a picosecond, which makes explicit approaches prohibitively expensive. These constraints were overcome in part by various approaches, such as fractional step methods [8,9], strong stability preserving (SSP) explicit schemes [10], semi-implicit methods [11,12], and even some implicit methods [13] with semi-implicit treatment of the potential. These methods are usually limited by less restrictive drift or dielectric time scales $\mathcal{O}(10^{-11}\text{-}~10^{-12}~\text{s})$. While time steps of size below the drift and dielectric time scales might be acceptable for the streamer propagation phase, they become a major inefficiency for simulations that consider multiple pulses preceding the formation of the streamer and multiple pulses after the streamer propagation at frequencies of 1 to 100 kHz.

The order of accuracy of the temporal integration can also influence the maximum allowable time step size. As mentioned, for explicit and some semi-implicit schemes, the time step size is limited by stability constraints. Because the step size is limited by stability rather than by accuracy, second-order temporal accuracy is often appropriate. Conversely, for implicit methods that can step over the typical drift, diffusion, and dielectric limits, the time step size is limited by accuracy. In this case, increasing the temporal order of accuracy is required to improve the efficiency of the solver.

Temporal integration with physically accurate boundary conditions at the electrodes also poses a major challenge. The use of realistic boundary conditions induces the formation of thin charge layers, which require high spatial resolution. The formation of the cathode sheath [14] is particularly impactful since it induces a peak electric field strength that is several times that encountered at the streamer head. Very refined meshes and high electric fields further decrease the drift time scale. Consequently, even recent studies [15,16] opt for boundary conditions that prevent the formation of the cathode sheath altogether.

The fully implicit treatment of the nonlinear system of partial differential equations that describes streamer propagation is uncommon in more than one dimension [17,18]. By fully implicit, we mean that the space-discrete form of the conservation equations for the plasma particles and Poisson equation for the potential induced by the space charge are integrated in time with a time-implicit method, whereby all variables are advanced to the next step at once.

A straightforward approach requires forming and factorizing many Jacobian matrices. For computational meshes consisting of millions of grid points or control volumes, this is not practical due to the cost of factorizing large matrices at every time step. The Jacobian-free Newton-Krylov (JFNK) [19] method overcomes this limitation by employing approximations to Jacobian-vector products that do not require the formation of the Jacobian matrix itself. Approximate Jacobians with desirable properties are used as preconditioners within an iterative Krylov linear solver. If the preconditioner is effective, such approach is computationally efficient as it reduces the number of iterations required for the solution of the linear system at each nonlinear Newton iteration, while benefitting from the stability properties and small error inherent to a high-order implicit time integration method. The greatest challenge in the efficient application of JFNK methods is that effective preconditioners are specific to the governing equations, requiring ad-hoc strategies and approaches.

Fully implicit JFNK methods and suitable preconditioners have been applied successfully to other stiff problems where it is necessary to circumvent the fastest time scales. Such problems include atmospheric flows [20], low-Mach variable-density flows in nuclear reactors [21], and magnetohydrodynamics (MHD) in the context of fusion-device modeling [22]. In the aforementioned cases, the solver retains the advantages of implicit integration (large time step sizes independent of spatial resolution), and is competitive with (and often superior to) explicit and semi-implicit methods over a wide range of conditions within a single framework.

In this work we develop a novel physics-based preconditioner [23–28] for a fully-coupled, fully implicit system of transport equations that describe the temporal and spatial evolution of electrons, positive ions, and negative ions during non-thermal plasma discharges. The preconditioner deals also with nonlinear numerical boundary conditions for charged species at the electrodes and is applied in the context of a JFNK method with high-order temporal integration for computational efficiency. Section 2 discusses the physical model, including transport equations, chemical kinetics, and boundary conditions. Section 3 deals with the spatial and temporal discretization of the partial differential equations. Section 4 provides an overview of the preconditioned JFNK solution approach. Section 5 provides an in-depth presentation of the preconditioning strategy, and remaining practical details are discussed in Section 6. The application and performance assessment of our novel preconditioner for two non-thermal plasma discharges are presented in 7 and parallel performance and scaling results are presented in Section 8. Conclusions follow in Section 9.

2. Physical model and governing equations

A three-particle, non-thermal plasma fluid model together with the local field approximation [29,30] is adopted. The particles are electrons, one class of positive ions, and one class of negative ions, each with unit charge. In our simplified model, the charged plasma particles interact with each other and with a background neutral gas, which has constant number density and constant temperature. In other words, plasma processes are assumed to have a negligible effect on

the background neutral gas. While such an assumption is problematic for high degrees of ionization and Joule heating, which induce changes in the thermo-chemical state of background gas, it is a convenient simplification that allows to focus on developing a numerical method for the solution of the plasma particles' conservation equations. The background gas is assumed to be capable of electron impact ionization, electron attachment, and of serving as third-body in ion-ion and electron-ion recombination processes. The ions are assumed to be in thermal equilibrium with the background gas, while electrons are non-thermal and attain much higher temperatures.

Henceforth, dimensional variables are denoted with a tilde, while dimensionless variables are expressed without the tilde. The governing equations are made dimensionless as follows. Lengths are made dimensionless by the Debye length $\tilde{\lambda}_0 = \sqrt{\tilde{\epsilon}_0 \tilde{k}_B \tilde{T}_0/\tilde{e}^2 \tilde{n}_0}$ evaluated at reference number density \tilde{n}_0 and reference temperature \tilde{T}_0 (specified in later sections). Here $\tilde{e}=1.602176634\times 10^{-19}$ C is the unit charge, $\tilde{\epsilon}_0=8.8541878128\times 10^{-12}$ Fm⁻¹ the permittivity in vacuum (unity relative permittivity is assumed), and $\tilde{k}_B=1.380649\times 10^{-23}$ JK⁻¹ is Boltzmann's constant. Time is made dimensionless by the plasma period $2\pi/\tilde{\omega}_0$, where $\tilde{\omega}_0=\sqrt{\tilde{e}^2\tilde{n}_0/\tilde{\epsilon}_0\tilde{m}_e}$ is the plasma frequency at reference number density \tilde{n}_0 and $\tilde{m}_e=9.1093837015\times 10^{-31}$ kg is the electron mass. The number densities of electrons and ions as well as of the neutral background gas are made dimensionless by \tilde{n}_0 . The electric field is made dimensionless by $\tilde{\lambda}_0\tilde{n}_0\tilde{e}/\tilde{\epsilon}_0$ and the electric potential by $\tilde{\lambda}_0^2\tilde{n}_0\tilde{e}/\tilde{\epsilon}_0$. The mean electron temperature is made dimensionless by the reference temperature \tilde{T}_0 . The reference degree of ionization is $\alpha_i=\tilde{n}_0/\tilde{N}_B$, where \tilde{N}_B is the constant number density of the neutral background gas with constant temperature \tilde{T}_B . Those are made dimensionless by \tilde{n}_0 and \tilde{T}_0 respectively.

For the sake of simplicity, we assume that the reduced electron mobility $\tilde{\mu}\tilde{N}_B$ is constant and that the reduced ion mobility $\tilde{\mu}_i\tilde{N}_B$ is the same for negative and positive ions and constant also. Einstein's relation is used to obtain diffusion coefficients from mobilities and temperatures of electrons and ions. We let $\tilde{\mu}\tilde{N}_B = 10^{24} \text{ V}^{-1} \text{ m}^{-1} \text{ s}^{-1}$ and $\tilde{\mu}_i\tilde{N}_B = 6.7 \times 10^{21} \text{ V}^{-1} \text{ m}^{-1} \text{ s}^{-1}$ as representative values of charge mobilities in air [31,32].

All physical constants, reference quantities, and variables describing the constant thermochemical state of the background gas are dimensional.

The dimensionless conservation equation for the electron number density $n = n(\mathbf{x}, t)$ is

$$\frac{\partial n}{\partial t} = a_1 \nabla \cdot (\theta n) + a_2 T_e \Delta n + \omega_i - \omega_{er} - \omega_a + \omega_d
= a_1 (\rho n + \theta \cdot \nabla n) + a_2 T_e \Delta n + \omega_i - \omega_{er} - \omega_a + \omega_d,$$
(1)

where \mathbf{x} is the position vector, t is time, and Δ is the Laplacian operator. The electric field vector is $\boldsymbol{\theta}$ with magnitude $\theta = |\boldsymbol{\theta}|$, $T_e = T_e(\theta)$ is the electron temperature, which is assumed to be a function of θ according to the local field approximation, and the contribution of ∇T_e to diffusion is neglected. Also, we let $\nabla \cdot \boldsymbol{\theta} = \rho$, where

$$\rho = u - v - n,\tag{2}$$

is proportional to the space charge density as all three plasma particles have unit charge. The terms ω_i , ω_{er} , ω_a , and ω_d represent the volumetric rates of electron ionization, electron-ion recombination, electron attachment, and electron detachment, respectively.

The dimensionless conservation equation for the number density of positive ions $u = u(\mathbf{x}, t)$ is

$$\frac{\partial u}{\partial t} = -a_7(\rho u + \theta \cdot \nabla u) + a_8 \Delta u + \omega_i - \omega_{er} - \omega_{ir},\tag{3}$$

where ω_{ir} represents the volumetric rate of ion-ion recombination.

The dimensionless conservation equation for the number density of negative ions $v = v(\mathbf{x}, t)$ is

$$\frac{\partial v}{\partial t} = a_7(\rho v + \boldsymbol{\theta} \cdot \nabla v) + a_8 \Delta v + \omega_a - \omega_{ir} - \omega_d. \tag{4}$$

The dimensionless electric field vector $\boldsymbol{\theta}$ is

$$\theta = \vartheta + \Theta, \tag{5}$$

where ϑ is the component due to the electric potential $\varphi(\mathbf{x},t)$ induced by the space charge

$$\vartheta = -\nabla \varphi,\tag{6}$$

and Θ is the component associated with the external electric potential $\Phi = \Phi(\mathbf{x}, t)$

$$\mathbf{\Theta} = -\nabla \Phi. \tag{7}$$

The electric potential induced by space charge obeys the Poisson equation

$$-\Delta \varphi = \rho,\tag{8}$$

and the external potential obeys the Laplace equation

$$-\Delta \Phi = 0. \tag{9}$$

Expressions for the dimensionless constants a_i and kinetics source terms, are discussed in Section 2.1. The partial differential equations are complemented by suitable boundary conditions, which are discussed in Section 2.2 for each discharge configuration considered.

2.1. Kinetic source terms closure

We are interested in streamer discharges in air near or above atmospheric pressure. The kinetic model for the three charged particles (electrons, cations, and anions) is inspired by the detailed air plasma kinetic model in Refs. [7,33] and complemented by electron detachment processes as in Refs. [34,35]. The objective is to obtain a simple kinetics mechanism that retains key features of plasmas formed in streamer discharges. Electron ionization is modeled as the impact ionization of molecular nitrogen $N_2 + e \longrightarrow N_2^+ + e + e$ and oxygen $O_2 + e \longrightarrow O_2^+ + e + e$ in air, electron-ion recombination is modeled as the dissociative recombination $e + O_2^+ \longrightarrow O_2 + O_2$, ion-ion recombination is modeled as the three-body attachment of electrons to molecular oxygen $e + O_2 + O_2 \longrightarrow O_2^- + O_2$, ion-ion recombination is modeled as the three-body recombination $O_2^+ + O_2^- + O_2 \longrightarrow O_2 + O_2 + O_2$, and electron detachment is modeled as $O_2^- + O_2 \longrightarrow O_2 + O_2 + e$. Thus, the positive ion represents the ensemble of nitrogen and oxygen cations, and the negative ion represents the oxygen anion. This simplified kinetic model was found to facilitate the development of numerical methods, while describing streamer ignition and propagation adequately.

Based on the above kinetic model, the source terms read

$$\omega_i = r_i n + S,\tag{10}$$

$$\omega_{er} = (a_5/T_e)un,\tag{11}$$

$$\omega_a = (a_6/T_e)n,\tag{12}$$

$$\omega_d = r_d \nu, \tag{13}$$

$$\omega_{ir} = a_9 v u. \tag{14}$$

The rate of ionization r_i is a function of the reduced electric field θ/N_B , and its functional form is from Ref. [31], which matches well with ionization rates in air (21% oxygen by volume and balancing nitrogen) calculated using BOLSIG+ with cross-sections from the Morgan database [36,37]. It is of the form

$$r_i = \tilde{k}_i (2\pi/\tilde{\omega}_0) \tilde{N}_B, \tag{15}$$

$$\tilde{k}_i = \tilde{f}_i(\tilde{\theta}/\tilde{N}_B). \tag{16}$$

Further details are provided in the Appendix. The term S represents a background source of volumetric ionization due to cosmic rays and radiation approximated as $\tilde{S} = 10^7 \text{ m}^{-3} \text{ s}^{-1}$ at atmospheric conditions [38,39]. The rate of electron detachment r_d is modeled as the sum of contributions at low electric fields (governed by the background temperature) and high electric fields [34,40]. It is of the form

$$r_d = \tilde{k}_d (2\pi/\tilde{\omega}_0) \tilde{N}_B, \tag{17}$$

$$\tilde{k}_d = 10^{f(\tilde{T}_B)} + 10^{g(\tilde{\theta}/\tilde{N}_B)}.$$
 (18)

Expressions for $f(\tilde{T}_B)$ and $g(\tilde{\theta}/\tilde{N}_B)$ are provided in the Appendix.

The dimensionless parameters a_i (i = 1, ..., 9) are

$$a_1 = (2\pi/\tilde{\omega}_0)\tilde{\mu}\tilde{N}_B\alpha_i\tilde{e}/\tilde{\epsilon}_0,\tag{19}$$

$$a_2 = a_1, \tag{20}$$

$$a_3 = (2\pi/\tilde{\omega}_0)\tilde{c}_8^a \tilde{N}_B,\tag{21}$$

$$a_4 = \tilde{c}_8^b \tilde{\epsilon}_0 / (\tilde{e}\alpha_i \tilde{\lambda}_0), \tag{22}$$

$$a_5 = (2\pi/\tilde{\omega}_0)\tilde{c}_{18}\tilde{n}_0(300/\tilde{T}_0),\tag{23}$$

$$a_6 = (2\pi/\tilde{\omega}_0)\tilde{c}_{19}\tilde{N}_B^2(300/\tilde{T}_0),\tag{24}$$

$$a_7 = (2\pi/\tilde{\omega}_0)\tilde{\mu}_i \tilde{N}_B \alpha_i \tilde{e}/\tilde{\epsilon}_0, \tag{25}$$

$$a_8 = a_7 \tilde{T}_B / \tilde{T}_0, \tag{26}$$

$$a_9 = (2\pi/\tilde{\omega}_0)\tilde{c}_{22}\tilde{n}_0\tilde{N}_B. \tag{27}$$

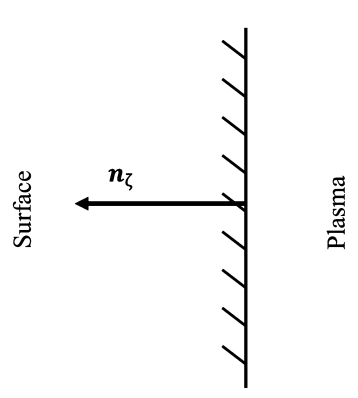


Fig. 1. Schematic of the local ζ coordinate in relation to the boundary surface and the domain occupied by the plasma.

The constants appearing in the parameters above are taken from select reactions in Refs. [7,33] and reflect the numbering convention therein: $\tilde{c}_8^a = 10^{-6} \exp(-8.3 \log 10) = 5.012 \times 10^{-15} \text{ m}^3 \text{ s}^{-1}$, $\tilde{c}_8^b = 8.301 \times 10^{-19} \text{ V m}^2$, $\tilde{c}_{18} = 2 \times 10^{-13} \text{ m}^3 \text{ s}^{-1}$, $\tilde{c}_{19} = 8.82 \times 10^{-43} \text{ m}^6 \text{ s}^{-1}$, and $\tilde{c}_{22} = 2 \times 10^{-37} \text{ m}^6 \text{ s}^{-1}$.

2.2. Boundary conditions

Boundary conditions at the electrode surfaces are taken from Ref. [41]. A Robin boundary condition is used for the number densities of electrons and ions as summarized briefly below. Note that velocities and speeds of all particles are made dimensionless by the reference velocity $\tilde{\lambda}_0 \tilde{\omega}_0 / 2\pi$ obtained dividing the reference length by the reference time.

The particle flux at electrode surfaces is driven by electric drift and diffusive processes. In the case of electrons, there is an additional term due to secondary emissions generated by the impact of ions on the surface of electrodes. Overall, these physical processes are modeled by Robin boundary conditions for a charged particle number density ψ

$$-D\frac{\partial \psi}{\partial \zeta} + V\psi = \chi,\tag{28}$$

where D is the diffusion coefficient (a_2T_e for electrons and a_8 for ions), V is the Hopf velocity combining thermal and electric drift processes, ζ is the local normal coordinate pointing away from the plasma and into the electrode as shown in Fig. 1, and χ represents the contribution of secondary particle emissions.

The Hopf velocity is defined as

$$V = |w| \pm a_i \theta_{\zeta},\tag{29}$$

where w is the dimensionless mean speed of the particle, a_i is the drift coefficient (a_1 for electrons and a_7 for ions), and $\theta_{\zeta} = \boldsymbol{\theta} \cdot \boldsymbol{n}_{\zeta}$ is the normal component of the electric field with the normal vector pointing in the direction shown in Fig. 1. The sign in Eq. (29) is positive for particles with negative charge and negative for particles with positive charge, consistent with the definition of the electric field.

For electrons, the dimensionless mean speed w_n is always equal to half the thermal velocity $c_{\text{mxw}}/2 = \sqrt{8\pi T_e}$. For ions, $w_{u,v}$ depends on the strength of the electric field [41]. Under the assumption of a weak field, the ion boundary conditions take a form similar to that of the electrons, with a thermal velocity calculated using the gas temperature T_B . Alternatively, under the limit of a strong field, the boundary condition is dominated by drift processes

$$|w_{u,v}| = \begin{cases} c_{\text{mxw}}^{u,v}/2 & \text{weak field,} \\ a_7|\theta| & \text{strong field.} \end{cases}$$
(30)

Secondary emissions are considered for electrons at the cathode only and read

$$\chi = 2\gamma \Gamma_u,\tag{31}$$

where γ is the secondary electron emissions coefficient and Γ_u is the flux of positive ions to the electrode defined as

$$\Gamma_{u} = |w_{u}|u, \tag{32}$$

where u is the number density of positive ions at the cathode. Reflections of electrons and ions at the electrodes are neglected.

For the electric potential, Dirichlet boundary conditions are specified on the surface of the electrodes. Finally, for all charged particles and electric potential, homogeneous Neumann conditions are specified on the axis for axisymmetric configurations and on the far-field of the computational boundary.

3. Temporal and spatial discretizations

3.1. Temporal semi-discrete form

The governing equations are integrated in time using an implicit multistep method based on Backward Differentiation Formulas (BDF), suitable for stiff systems of ordinary differential equations and differential algebraic equations of index 1 [42].

We adopt the *fixed-leading coefficient* form [43–45] of a variable step size q-step BDF method and define the approximation y^n to the solution of an initial value problem (IVP) at t_n as the solution to the difference equation

$$\sum_{j=0}^{q+1} \alpha_j^n y^{n-j} = h_n f(t_n, y^n), \tag{33}$$

where y^{n-j} are approximations to the solution of the IVP dy/dt = f(t,y) with $y(t_0) = y_0$ at time steps t_{n-j} ($j = 1, \ldots, q, q+1$), $h_n = t_n - t_{n-1}$ is the current step size, and the coefficients α_j^n are such that the left-hand-side of Eq. (33) approximates the derivative dy/dt at t_n to order q. This order condition determines uniquely α_j^n as function of the step size ratios h_j/h_{j-1} . Note that α_0 is a constant coefficient, which depends on the order of the BDF method, but is independent of the time step size history.

For simplicity, we rewrite Eq. (33) as

$$\alpha_0 y^n - \hat{y}^n = h_n f(t_n, y^n), \tag{34}$$

where we let

$$\hat{y}^n = -\sum_{i=1}^{q+1} \alpha_j^n y^{n-j}.$$
 (35)

The governing equation for the number density of electrons $n^n(\mathbf{x}) = n(\mathbf{x}, t_n)$ in fully implicit semi-discrete form reads

$$h_n^{-1}(\alpha_0 n^n - \hat{n}^n) = a_1(\rho^n n^n + \theta^n \cdot \nabla n^n) + a_2 T_e^n \Delta n^n + r_3^n n^n - r_5^n u^n n^n - r_6^n n^n + r_{10} v^n + S.$$
(36)

The equation for the number density of positive ions $u^n(\mathbf{x}) = u(\mathbf{x}, t_n)$ is

$$h_n^{-1}(\alpha_0 u^n - \hat{u}^n) = -a_7(\rho^n u^n + \theta^n \cdot \nabla u^n) + a_8 \Delta u^n + r_3^n n^n - r_5^n u^n n^n - a_9 v^n u^n + S,$$
(37)

and, similarly, for the number density of negative ions $v^n(\mathbf{x}) = v(\mathbf{x}, t_n)$

$$h_n^{-1}(\alpha_0 v^n - \hat{v}^n) = a_7(\rho^n v^n + \theta^n \cdot \nabla v^n) + a_8 \Delta v^n + r_6^n n^n - a_9 v^n u^n - r_{10} v^n.$$
(38)

In the above equations, we defined

$$\rho^n = u^n - v^n - n^n, \tag{39}$$

$$T_{e}^{n} = T_{e}(\theta^{n}), \tag{40}$$

$$r_2^n = r_i(\theta^n), \tag{41}$$

$$r_5^n = r_5(T_e^n) = a_5/T_e^n,$$
 (42)

$$r_6^n = r_6(T_e^n) = a_6/T_e^n,$$
 (43)

$$r_{10}^n = r_d(\theta^n).$$
 (44)

The electric field $\theta^n(\mathbf{x}) = \theta(\mathbf{x}, t_n)$ is defined as

$$\boldsymbol{\theta}^n = -\nabla \varphi^n + \mathbf{\Theta}(\mathbf{x}, t_n), \tag{45}$$

with $\varphi^n(\mathbf{x}) = \varphi(\mathbf{x}, t_n)$ the space charge electric potential such that

$$-\Delta \varphi^n = \rho^n. \tag{46}$$

Its magnitude is $\theta^n = |\boldsymbol{\theta}^n|$.

Together with suitable conditions on the boundary of the computational domain, Eqs. (36), (37), (38), (46), and (45) are a system of coupled nonlinear and linear partial differential equations for n^n , u^n , v^n , and φ^n to be solved in the computational domain Ω at each time step. The system of differential equations is complemented by closures for the electron temperature (40) and rate constants (41), (42), (43), and (44).

3.2. Spatial discretization with finite difference formulas

The continuous fields n^n , u^n , v^n , and φ^n are discretized in space on a finite difference mesh. Upon spatial discretization, the system of partial differential equations is transformed into a system of algebraic equations for the unknown vectors \underline{n}^n , \underline{u}^n , \underline{v}^n , and $\underline{\varphi}^n$, representing the solution at a finite number of grid points located in the interior of the domain and on its boundary. Henceforth, \mathcal{S}_Ω and $\mathcal{S}_{\partial\Omega}$ represent the sets of indices referring to interior and boundary points, respectively. The cardinality of \mathcal{S}_Ω is M^Ω , that of $\mathcal{S}_{\partial\Omega}$ is $M^{\partial\Omega}$, and $M=M^\Omega+M^{\partial\Omega}$ is the overall number of grid points.

The Laplacian and gradient operators are approximated by finite difference formulas:

$$\Delta y \approx \mathbb{L} y$$
, (47)

$$\nabla y \approx \mathbb{G} y,\tag{48}$$

and

$$\boldsymbol{\theta} \cdot \nabla y \approx (\boldsymbol{\theta} \cdot \mathbb{G}^{\pm}) y = \mathbb{D}^{\pm} y, \tag{49}$$

where y = y(x) is a continuous field and y its discrete restriction on a finite number of grid points.

The notation in Eq. (49) indicates that, if needed, the discrete approximation to the electric drift operator $\theta \cdot \nabla$ features upwinding of the finite difference formulas based on the local direction of the electric field vector, which governs that of the local charge drift velocity. The upwind direction is opposite for positive (+) and negative (-) charges. Thus, if upwinding is employed, the discrete drift operator $\mathbb{D}^{\pm} = \mathbb{D}^{\pm}(\theta)$ is a function of the electric field vector and different for positive and negative charges. It is noted that all simulations presented in Section 7 did not use upwind finite difference formulas, relying instead on non-dissipative centered second order finite difference approximations to the gradient operator.

The resulting system of algebraic equations at interior grid points reads

$$h_{n}^{-1}(\alpha_{0}\underline{n}^{n} - \underline{\hat{n}}^{n}) = f_{n}(t_{n}; \underline{n}^{n}, \underline{\nu}^{n}, \underline{\nu}^{n}, \underline{\varphi}^{n})$$

$$= a_{1}[\rho^{n} + \mathbb{D}^{-}(\theta^{n})]\underline{n}^{n} + a_{2}T_{e}^{n}\underline{\mathbb{L}}\underline{n}^{n}$$

$$+ r_{3}^{n}\underline{n}^{n} - r_{5}^{n}\underline{u}^{n}\underline{n}^{n} - r_{6}^{n}\underline{n}^{n} + r_{10}\underline{\nu}^{n} + S,$$

$$(50)$$

$$h_{n}^{-1}(\alpha_{0}\underline{u}^{n} - \underline{\hat{u}}^{n}) = f_{u}(t_{n}; \underline{n}^{n}, \underline{u}^{n}, \underline{\nu}^{n}, \underline{\varphi}^{n})$$

$$= -a_{7}[\rho^{n} + \mathbb{D}^{+}(\theta^{n})]\underline{u}^{n} + a_{8}\underline{\mathbb{L}}\underline{u}^{n}$$

$$+ r_{3}^{n}\underline{n}^{n} - r_{5}^{n}\underline{u}^{n}\underline{n}^{n} - a_{9}\underline{\nu}^{n}\underline{u}^{n} + S,$$

$$h_{n}^{-1}(\alpha_{0}\underline{\nu}^{n} - \underline{\hat{\nu}}^{n}) = f_{\nu}(t_{n}; \underline{n}^{n}, \underline{u}^{n}, \underline{\nu}^{n}, \underline{\varphi}^{n})$$

$$= a_7 [\rho^n + \mathbb{D}^-(\boldsymbol{\theta}^n)] \underline{v}^n + a_8 \mathbb{L} \underline{v}^n + r_6^n n^n - a_9 v^n u^n - r_{10} v^n,$$
(52)

and

$$0 = f_{\varphi}(\underline{n}^{n}, \underline{u}^{n}, \underline{v}^{n}, \underline{\varphi}^{n}),$$

= $\mathbb{L}\underline{\varphi}^{n} + \rho^{n}$. (53)

Here $\rho^n = \underline{u}^n - \underline{v}^n - \underline{n}^n$.

Given φ^n and the external electric field at time t_n , the electric field vector at each grid point is

$$\boldsymbol{\theta}^{n} = \boldsymbol{\theta}^{n}(\varphi^{n}) = -\mathbb{G}\varphi^{n} + \boldsymbol{\Theta}(\boldsymbol{x}, t_{n}). \tag{54}$$

The electron temperature T_e^n and rate constants are evaluated at each grid point given the magnitude of the electric field vector, $\theta^n = |\theta^n|$.

Numerical boundary conditions for plasma discharge modeling involve the value of the electric field and number density of charges as well as discrete approximations to their spatial derivatives at grid points on the domain boundary $\partial\Omega$. They take the form of nonlinear algebraic equations that complement the system of equations above, which apply to interior grid points only. Regardless of their functional form, they are written

$$g_n(t_n; \underline{n}^n, \underline{u}^n, \underline{v}^n, \varphi^n) = 0, \tag{55}$$

$$g_u(t_n; \underline{n}^n, \underline{u}^n, \underline{v}^n, \varphi^n) = 0, \tag{56}$$

$$g_{\nu}(t_n; \underline{n}^n, \underline{u}^n, \underline{\nu}^n, \varphi^n) = 0, \tag{57}$$

$$g_{\varphi}(t_n; \underline{n}^n, \underline{u}^n, \underline{v}^n, \varphi^n) = 0. \tag{58}$$

It is important to note that, due to the coupling between electric field and space charge in the computational domain Ω , the numerical boundary conditions depend on the number density of electrons and ions at all grid points.

4. Jacobian-free Newton-Krylov with PGMRES iterative solver

Advancing the discrete fields from time t_{n-1} to t_n requires solving a large system of nonlinear algebraic equations. If M is the number of grid points (interior plus boundary points), then the system of equations has dimensionality equal to 4M due to the coupling between the three charge number density fields and electric potential induced by the space charge. The task of solving such system is computationally challenging, especially in two- and three-dimensional configurations, when $M \sim \mathcal{O}(10^5 - 10^9)$ for practical problems.

We manipulate the system of algebraic equations and define nonlinear residual functions

$$F_n(n, u, v, \varphi) = h_n^{-1}(\alpha_0 n - \hat{n}^n) - f_n(t_n; n, u, v, \varphi),$$
(59)

$$F_u(n, u, v, \varphi) = h_n^{-1}(\alpha_0 u - \hat{u}^n) - f_u(t_n; n, u, v, \varphi), \tag{60}$$

$$F_{\nu}(\mathbf{n}, \mathbf{u}, \mathbf{v}, \varphi) = h_n^{-1}(\alpha_0 \mathbf{v} - \hat{\mathbf{v}}^n) - f_{\nu}(t_n; \mathbf{n}, \mathbf{u}, \mathbf{v}, \varphi), \tag{61}$$

$$F_{\varphi}(\mathbf{n}, \mathbf{u}, \mathbf{v}, \varphi) = -f_{\varphi}(\mathbf{n}, \mathbf{u}, \mathbf{v}, \varphi), \tag{62}$$

for interior grid points and

$$G_n(\mathbf{n}, \mathbf{u}, \mathbf{v}, \varphi) = -g_n(t_n; \mathbf{n}, \mathbf{u}, \mathbf{v}, \varphi), \tag{63}$$

$$G_u(n, u, v, \varphi) = -g_u(t_n; n, u, v, \varphi),$$
 (64)

$$G_{\nu}(n, u, v, \varphi) = -g_{\nu}(t_n; n, u, v, \varphi),$$
 (65)

$$G_{\omega}(\mathbf{n}, \mathbf{u}, \mathbf{v}, \varphi) = -g_{\omega}(t_{\mathbf{n}}; \mathbf{n}, \mathbf{u}, \mathbf{v}, \varphi), \tag{66}$$

for boundary points, where n, u, v, and ϕ are dummy (vector) variables.

For the sake of notational convenience, we define the (column) state vector

$$\mathbf{q} = (\mathbf{n}, \mathbf{u}, \mathbf{v}, \mathbf{\phi})^T, \tag{67}$$

and nonlinear (column) residual vector

$$\mathbf{F} = (F_n, F_u, F_v, F_{\varphi}, G_n, G_u, G_v, G_{\varphi})^T, \tag{68}$$

such that the system of algebraic equations to be solved at each time step is

$$\mathbf{F}(\mathbf{q}) = 0. \tag{69}$$

Newton's method is used to solve $F(\mathbf{q}) = 0$ iteratively to obtain \underline{n}^n , \underline{u}^n , \underline{v}^n , and $\underline{\varphi}^n$. At each nonlinear iteration k, the linear system

$$\mathbf{J}^{k-1}\delta\mathbf{q}^k = -\mathbf{F}(\mathbf{q}^{k-1}),\tag{70}$$

is solved, where $J^{k-1} = J(q^{k-1})$ is the Jacobian matrix of F(q) evaluated at state q^{k-1} and δq^k is the update to the state vector

$$\mathbf{q}^k = \mathbf{q}^{k-1} + \delta \mathbf{q}^k. \tag{71}$$

Newton's method is started with a guess q^0 .

Due to its large size, J is not formed and explicitly available for use as in direct methods. Instead, we employ the preconditioned generalized minimum residual (PGMRES) iterative method [46] together with a first-order Taylor approximation to the product of vector \mathbf{v} with Jacobian J.

$$J(q)v \approx \frac{F(q+\epsilon v) - F(q)}{\epsilon},\tag{72}$$

where ϵ is a small parameter [23].

The solution of the linear system in Eq. (70) via iterative methods is computationally practical only if an effective preconditioner is used. An effective preconditioner P closely resembles J^{k-1} , while being much easier to invert than J^{k-1} itself. One then solves the problem

$$(\boldsymbol{J}^{k-1}\boldsymbol{P}^{-1})\boldsymbol{z} = -\boldsymbol{F}(\boldsymbol{q}^{k-1}) \tag{73}$$

for z, followed by

$$\mathbf{P}\delta\mathbf{q}^k = \mathbf{z} \tag{74}$$

for δq^k . On the account that P is close to J^{k-1} , the matrix product $J^{k-1}P^{-1}\approx I$, and the first problem is trivial. The second problem is also more efficiently solved than the original linear system as long as P has desirable numerical properties, as is the case with an effective preconditioner.

In *matrix-free* implementations of PGMRES, whereby neither J^{k-1} nor P are formed, preconditioning requires the solution to the linear system

$$\mathbf{P}\mathbf{w} = \mathbf{r},\tag{75}$$

for w given some vector r at each Krylov iteration. The key to effective preconditioning is to ensure that the solution to Pw = r is computationally efficient, while guaranteeing that P is as close as possible to J^{k-1} . In practice, this usually involves formulating P as a matrix with smaller independent blocks that are easy to invert.

The main contribution of our work is the development and evaluation of a robust and efficient preconditioner for plasma discharges based on the theory of physics-based, operator-splitting preconditioning [23–28].

5. Physics-based, operator-splitting preconditioner for plasma discharges

The idea behind the class of physics-based, operator-split preconditioners is to seek simplifications to the residual vector function \mathbf{F} by (i) linearization of the nonlinear terms and (ii) decoupling of the unknowns inspired by classical operator-splitting approaches. For an overview of such approaches, the reader is referred to the review in Ref. [19].

5.1. Linearization of the residual vector function

We proceed to formulate \widetilde{F} , a linear approximation to F based on an expansion centered at state q^{\bullet} and evaluated at nearby state $q = q^{\bullet} + \delta q$. Products ab are approximated as

$$ab = (a^{\bullet} + \delta a)(b^{\bullet} + \delta b) \approx a^{\bullet}b^{\bullet} + a^{\bullet}\delta b + b^{\bullet}\delta a, \tag{76}$$

and all remaining nonlinear functions of \boldsymbol{q} are evaluated at \boldsymbol{q}^{\bullet} for simplicity. The only exception is the linearization of products of the form $\rho\psi$ where ψ is the number density of any charged particle. These products are simplified as $\rho\psi = \rho^{\bullet}(\psi^{\bullet} + \delta\psi)$ in order to avoid the split treatment of any drift term as seen in Section 5.2. For example, the linear approximation to the residual function of electrons at interior grid points reads

$$F_{n}(t_{n}; \boldsymbol{q}) \approx \widetilde{F}_{n}(t_{n}, \boldsymbol{q}^{\bullet}; \delta \boldsymbol{q}) = F_{n}(t_{n}; \boldsymbol{q}^{\bullet}) + [h_{n}^{-1}\alpha_{0} - a_{1}\rho^{\bullet} - a_{1}\mathbb{D}^{\bullet, -} - a_{2}T_{e}^{\bullet}\mathbb{L} - r_{3}^{\bullet} + r_{5}^{\bullet}\mathbf{u}^{\bullet} + r_{6}^{\bullet}]\delta \mathbf{n} + (r_{5}^{\bullet}\mathbf{n}^{\bullet})\delta \mathbf{u} - (r_{10}^{\bullet})\delta \mathbf{v},$$

$$(77)$$

where we defined

$$\rho^{\bullet} = \mathbf{u}^{\bullet} - \mathbf{v}^{\bullet} - \mathbf{n}^{\bullet},\tag{78}$$

and the electron temperature T_e^{\bullet} and rates r_3^{\bullet} , r_5^{\bullet} , r_5^{\bullet} , r_6^{\bullet} , and r_{10}^{\bullet} are computed at T_e^{\bullet} and $\theta^{\bullet} = |\theta^{\bullet}|$ with the electric field vector defined as

$$\boldsymbol{\theta}^{\bullet} = -\mathbb{G}\,\boldsymbol{\varphi}^{\bullet} + \boldsymbol{\Theta}(\boldsymbol{x}, t_n). \tag{79}$$

Similarly, $\mathbb{D}^{\bullet,\pm} = \mathbb{D}^{\pm}(\boldsymbol{\theta}^{\bullet})$.

Linearization yields similar equations for positive ions

$$F_{u}(t_{n}; \mathbf{q}) \approx \widetilde{F}_{u}(t_{n}, \mathbf{q}^{\bullet}; \delta \mathbf{q}) = F_{u}(t_{n}; \mathbf{q}^{\bullet}) + [h_{n}^{-1}\alpha_{0} + a_{7}\rho^{\bullet} + a_{7}\mathbb{D}^{\bullet,+} \\ -a_{8}\mathbb{L} + r_{5}^{\bullet}\mathbf{n}^{\bullet} + a_{9}\mathbf{v}^{\bullet}]\delta\mathbf{u} - (r_{3}^{\bullet} - r_{5}^{\bullet}\mathbf{u}^{\bullet})\delta\mathbf{n} \\ - (-a_{9}\mathbf{u}^{\bullet})\delta\mathbf{v},$$

$$(80)$$

and negative ions

$$F_{\nu}(t_n; \boldsymbol{q}) \approx \widetilde{F}_{\nu}(t_n, \boldsymbol{q}^{\bullet}; \delta \boldsymbol{q}) = F_{\nu}(t_n; \boldsymbol{q}^{\bullet}) + [h_n^{-1}\alpha_0 - a_7\rho^{\bullet} - a_7\mathbb{D}^{\bullet, -} - a_8\mathbb{L} + a_9\mathbf{u}^{\bullet} + r_{10}^{\bullet}]\delta\mathbf{v} - (r_{6}^{\bullet})\delta\mathbf{n} - (-a_9\mathbf{v}^{\bullet})\delta\mathbf{u},$$

$$(81)$$

at interior grid points.

The residual function associated with the space charge potential at interior points is unchanged as it is linear

$$F_{\varphi}(t_n; \boldsymbol{q}) = \widetilde{F}_{\varphi}(t_n, \boldsymbol{q}^{\bullet}; \delta \boldsymbol{q}) = F_{\varphi}(t_n; \boldsymbol{q}^{\bullet}) - \mathbb{L}\delta\varphi - (\delta \mathbf{u} - \delta \mathbf{v} - \delta \mathbf{n}). \tag{82}$$

Although expressions are not given here, similar linearizations are required for the residual functions pertaining to the numerical boundary conditions, yielding $\widetilde{G}_n(t_n, \boldsymbol{q}^{\bullet}; \delta \boldsymbol{q})$ and similarly for \widetilde{G}_u , \widetilde{G}_v , and \widetilde{G}_{φ} .

Setting

$$\widetilde{\mathbf{F}} = (\widetilde{F}_n, \widetilde{F}_u, \widetilde{F}_v, \widetilde{F}_{\varphi}, \widetilde{G}_n, \widetilde{G}_u, \widetilde{G}_v, \widetilde{G}_{\varphi})^T = 0$$
(83)

gives a linear system for $\delta \mathbf{q} = (\delta \mathbf{n}, \delta \mathbf{u}, \delta \mathbf{v}, \delta \mathbf{\varphi})$ with known vector $-\mathbf{F}(t_n; \mathbf{q}^{\bullet})$. Effectively, we obtained a linear approximation to the original nonlinear system, which can be used as a preconditioner provided it can be solved efficiently.

5.2. Application of the preconditioner via operator-splitting

The linearized problem consistent with Newton's method consists in the product of Jacobian matrix and the Newton update being equal to negative of the residual

$$\begin{bmatrix}
\frac{\partial F_{n}/\partial n}{\partial F_{u}/\partial n} & \frac{\partial F_{n}/\partial u}{\partial F_{u}/\partial u} & \frac{\partial F_{n}/\partial v}{\partial F_{u}/\partial v} & \frac{\partial F_{n}/\partial \theta}{\partial \theta} \cdot \frac{\partial \theta}{\partial \varphi} \\
\frac{\partial F_{u}/\partial n}{\partial F_{v}/\partial n} & \frac{\partial F_{u}/\partial u}{\partial F_{v}/\partial u} & \frac{\partial F_{u}/\partial \theta}{\partial F_{v}/\partial v} & \frac{\partial F_{v}/\partial \theta}{\partial \theta} \cdot \frac{\partial \theta}{\partial \varphi} \\
I & -I & \mathbb{L}
\end{bmatrix}
\begin{bmatrix}
\delta n \\ \delta u \\ \delta v \\ \delta \varphi
\end{bmatrix} = \begin{bmatrix}
-F_{n} \\ -F_{u} \\ -F_{v} \\ -F_{\varphi}
\end{bmatrix}.$$
(84)

An effective preconditioner requires that it be easy to invert, which is the case when unknowns are loosely coupled. For example, the linearization described in the previous section neglects the coupling between δn , δu , δv and $\delta \phi$ because the electric field induced by the space charge is approximated by that associated with the potential ϕ^{\bullet} , rather than $\phi = \phi^{\bullet} + \delta \phi$. Consequently, all nonlinear quantities that depend on the electric field and appear in the equations for the number densities of charges are constant when the linearization is applied, resulting in the approximate Jacobian

$$\mathbb{J}^{\bullet} = \begin{bmatrix} \frac{\partial F_{n}^{\bullet}/\partial n}{\partial F_{n}^{\bullet}/\partial n} & \frac{\partial F_{n}^{\bullet}/\partial v}{\partial F_{n}^{\bullet}/\partial u} & \frac{\partial F_{n}^{\bullet}/\partial v}{\partial F_{n}^{\bullet}/\partial u} & \frac{\partial F_{n}^{\bullet}/\partial v}{\partial F_{n}^{\bullet}/\partial v} & 0\\ \frac{\partial F_{n}^{\bullet}/\partial n}{\partial F_{n}^{\bullet}/\partial n} & \frac{\partial F_{n}^{\bullet}/\partial v}{\partial F_{n}^{\bullet}/\partial v} & 0\\ I & -I & I & \mathbb{L} \end{bmatrix} = \begin{bmatrix} 0\\ \mathbb{A}^{\bullet} & 0\\ 0\\ I & -I & I & \mathbb{L} \end{bmatrix}. \tag{85}$$

Inspection of $\widetilde{\mathbf{F}}$ shows that there is coupling among components δn , δu , and δv due to both reactions and space charge effects represented by block \mathbb{A}^{\bullet} . Such coupling is computationally costly because it implies that a system of 3M equations and 3M unknowns must be solved every time the preconditioner is applied. The situation is even more challenging for plasma models that feature more than three charged particles, as is often the case for high-fidelity chemical plasma kinetic models. Here, we work around this requirement by implementing an operator-splitting approach to approximate \mathbb{A}^{\bullet} , whereby select terms in the linear system are segregated and handled independently one from the other upon the introduction of intermediate solution vectors. Then, the inversion of the preconditioner is approximated by solving smaller linear systems sequentially, which is computationally advantageous. Thus, we let $\mathbb{A}^{\bullet} = \mathbb{A}^{\bullet}_1 + \mathbb{A}^{\bullet}_2$, where $\mathbb{A}^{\bullet}_1 = \mathbb{D}^{\bullet} + \mathbb{L} + \operatorname{diag}(\mathbb{R}^{\bullet})$ and $\mathbb{A}^{\bullet}_2 = \mathbb{R}^{\bullet} - \operatorname{diag}(\mathbb{R}^{\bullet})$. Here \mathbb{D} , \mathbb{L} , and \mathbb{R} represent the drift, Laplacian, and reaction operators respectively. The reduced blocks are represented by

$$\mathbb{A}^{\bullet} = \mathbb{A}_{1}^{\bullet} + \mathbb{A}_{2}^{\bullet}, \tag{86}$$

$$\mathbb{A}_{1}^{\bullet} = \begin{bmatrix} \partial F_{n}^{\bullet} / \partial n & 0 & 0 \\ 0 & \partial F_{\nu}^{\bullet} / \partial u & 0 \\ 0 & 0 & \partial F_{\nu}^{\bullet} / \partial v \end{bmatrix} = \begin{bmatrix} P_{n} & 0 & 0 \\ 0 & P_{u} & 0 \\ 0 & 0 & P_{v} \end{bmatrix}, \tag{87}$$

$$\mathbb{A}_{2}^{\bullet} = \begin{bmatrix} 0 & \partial F_{n}^{\bullet} / \partial u & \partial F_{n}^{\bullet} / \partial v \\ \partial F_{u}^{\bullet} / \partial n & 0 & \partial F_{u}^{\bullet} / \partial v \\ \partial F_{v}^{\bullet} / \partial n & \partial F_{v}^{\bullet} / \partial u & 0 \end{bmatrix}. \tag{88}$$

If the matrix \mathbb{A}_2^{\bullet} is reconfigured for the alternate ordering $(n_1, u_1, v_1, n_2, u_2, v_2, ..., n_N, u_N, v_N,)^T$, the solution to the approximate linear system is obtained by solving N independent blocks Q_i of size 3×3

$$\mathbb{A}_{2}^{\bullet} = \begin{bmatrix} Q_{1}^{\bullet} & 0 & 0 & 0 & \dots & 0 \\ 0 & Q_{2}^{\bullet} & 0 & 0 & \dots & 0 \\ \vdots & \dots & \ddots & \dots & \dots & \vdots \\ \vdots & \dots & \dots & Q_{i}^{\bullet} & \dots & 0 \\ \vdots & \dots & \dots & \dots & \ddots & \vdots \\ 0 & 0 & 0 & \dots & 0 & Q_{N}^{\bullet} \end{bmatrix}.$$

$$(89)$$

The application of the preconditioner is then summarized as follows, where \mathbb{P} is a permutation matrix

$$[\delta n, \delta u, \delta v]^{T} = \mathbb{P}^{-1}(\mathbb{A}_{2}^{\bullet})^{-1}\mathbb{P}(h^{-1}\alpha_{0}(\mathbb{A}_{1}^{\bullet})^{-1}[-F_{n}, -F_{u}, -F_{v}]^{T}), \tag{90}$$

$$\delta \varphi = \mathbb{L}^{-1}[(\delta \mathbf{u} - \delta \mathbf{n} - \delta \mathbf{v}) - F_{\varphi}]. \tag{91}$$

In practice, we take advantage of the block structure of \mathbb{A}_1^{\bullet} and \mathbb{A}_2^{\bullet} to invert the matrices and solve the corresponding linear systems efficiently.

As discussed, the application of a preconditioner matrix P requires the solution to Pw = r at each Krylov iteration. Here r is a known vector, in general different for each Krylov iteration, and w is the solution vector. In what follows, we let r^n , r^u , r^v , r^φ , and similarly, w^n , w^u , w^v , and w^φ indicate the restriction of known vector r and solution vector w to the elements corresponding to the respective variables (electrons, positive ions, negative ions, and electric potential) in q. The preconditioning strategy is outlined below and summarized in Algorithm 1. First, the linear system

$$\underbrace{\left[h_n^{-1}\alpha_0 - \left(a_2 T_e^{\bullet} \mathbb{L} + a_1 \mathbb{D}^{-,\bullet} + a_1 \rho^{\bullet} + r_3^{\bullet} - r_5^{\bullet} \mathbf{u}^{\bullet} - r_6^{\bullet}\right)\right]}_{P_n} w_*^n = -r^n, \tag{92}$$

is solved for w_*^n given r^n . Similarly, the linear system

$$\underbrace{[h_n^{-1}\alpha_0 - (a_8\mathbb{L} - a_7\mathbb{D}^{+,\bullet} - a_7\rho^{\bullet} - r_5^{\bullet}\mathbf{n}^{\bullet} - a_9^{\bullet}\mathbf{v}^{\bullet})]}_{P_u} w_*^u = -r^u, \tag{93}$$

is solved for w_*^u given r^u and

$$\underbrace{[h_n^{-1}\alpha_0 - (a_8\mathbb{L} + a_7\mathbb{D}^{-,\bullet} + a_7\rho^{\bullet} - a_9^{\bullet}\mathbf{u} - r_{10}^{\bullet})]}_{P_{\nu}} w_*^{\nu} = -r^{\nu}, \tag{94}$$

for w_*^{ν} given r^{ν} . In essence, the linear system for each species contains all diagonal elements with no distinction between drift, diffusion, and reaction terms. The only off-diagonal elements are due to space-discrete approximations to drift and diffusion operators. This initial step corresponds to lines 4 to 6 in Algorithm 1.

Although not presented explicitly here, linear and segregated equations are formulated for the unknowns at boundary points also. These equations are consistent with the linearized residual functions for the boundary points and are solved together with each of the three systems above, yielding three independent linear systems of size *M*. Examples are discussed in Section 7 for specific configurations.

Second, once the intermediate solutions w_*^n , w_*^u , and w_*^v are available, M^{Ω} independent 3×3 linear systems are solved for w_i^n , w_i^u , and w_i^v

$$h_n^{-1}\alpha_0 w_{*,i}^n = h_n^{-1}\alpha_0 w_i^n + (r_5^{\bullet} \mathbf{n}^{\bullet}) w_i^u + (-r_{10}^{\bullet}) w_i^v, \tag{95}$$

$$h_n^{-1}\alpha_0 w_{*,i}^u = (r_5^{\bullet} \mathbf{u}^{\bullet} - r_3^{\bullet}) w_i^n + h_n^{-1}\alpha_0 w_i^u + (a_9 \mathbf{u}^{\bullet}) w_i^v,$$
(96)

$$h_n^{-1}\alpha_0 w_{*,i}^{\nu} = (-r_6^{\bullet})w_i^n + (a_9 v^{\bullet})w_i^u + h_n^{-1}\alpha_0 w_i^{\nu}, \tag{97}$$

at interior point $i \in \mathcal{S}_{\Omega}$. Conversely, we let $w_i^n = w_{*,i}^n$, $w_i^u = w_{*,i}^u$, and $w_i^v = w_{*,i}^v$ at boundary point $i \in \mathcal{S}_{\partial\Omega}$. These additional linear systems are composed of mixed terms arising from the remaining kinetic coupling among species, and can be easily extended to an arbitrary number of reactions. This step corresponds to the "for-loop" in lines 7 to 10 in Algorithm 1. In matrix form

$$\underbrace{\begin{bmatrix} h_{n}^{-1}\alpha_{0} & (r_{5}^{\bullet}n^{\bullet}) & (-r_{10}^{\bullet}) \\ (r_{5}^{\bullet}u^{\bullet} - r_{3}^{\bullet}) & h_{n}^{-1}\alpha_{0} & (a_{9}u^{\bullet}) \\ (-r_{6}^{\bullet}) & (a_{9}v^{\bullet}) & h_{n}^{-1}\alpha_{0} \end{bmatrix}}_{O_{i}} \begin{bmatrix} w_{i}^{n} \\ w_{i}^{u} \\ w_{i}^{v} \end{bmatrix} = h_{n}^{-1}\alpha_{0} \begin{bmatrix} w_{*,i}^{n} \\ w_{*,i}^{u} \\ w_{*,i}^{v} \end{bmatrix}, \tag{98}$$

we let Q indicate the block diagonal matrix composed of all 3×3 blocks Q_i . Finally, vector w^{φ} is obtained solving

$$\mathbb{L}w^{\varphi} = (w^u - w^n - w^v) - r^{\varphi} \tag{99}$$

for all interior points $i \in S_{\Omega}$. At boundary points $i \in S_{\partial\Omega}$ the entries of operator $\mathbb L$ in Eq. (99) and its corresponding right-hand side are modified to enforce homogeneous Dirichlet conditions at the electrodes and homogeneous Neumann conditions at the axis and far-field boundaries. Note that the resulting matrix P_{φ} does not depend on the state vector \mathbf{q} . This final step corresponds to lines 11 to 12 in Algorithm 1. The selection of a suitable state \mathbf{q}^{\bullet} to form matrices P_n , P_u , P_v , and Q is discussed in Section 6.2. The order of the operators during preconditioning plays an important role in the performance of the solver, and the authors experimented with alternative orderings and also swapping select elements in the operators. The best performance was achieved with the strategy presented in this Section.

Algorithm 1 Preconditioning Algorithm.

```
1: procedure Precondition(r, w)
               Input:r=(r^n, r^u, r^v, r^{\varphi})^T
               Output: w = (w^n, w^u, w^v, w^{\varphi})^T
  3:
               w_*^n \leftarrow \text{solve } P_n w_*^n = -r^n;
                                                                                                                                                                                                                                                                    ⊳ Solve 3 linear systems size M
               w_*^u \leftarrow \text{solve } P_u w_*^u = -r^u;

w_*^v \leftarrow \text{solve } P_v w_*^v = -r^v;
  5:
  6:
               for i \in M^{\Omega} do
  7:
                                                                                                                                                                                                                                                   \triangleright Inner points only, local 3 \times 3 systems
                     b_{i} = h_{n}^{-1}\alpha_{0} (w_{*,i}^{n}, w_{*,i}^{u}, w_{*,i}^{v})^{T}; 
(w_{i}^{n}, w_{i}^{u}, w_{i}^{v})^{T} \longleftarrow \text{solve } Q_{i}(w_{i}^{n}, w_{i}^{u}, w_{i}^{v})^{T} = b_{i};
 8:
 9:
10:
               \begin{array}{l} w^{\varphi} \longleftarrow \text{solve } P_{\varphi}w^{\varphi} \text{=} (w^{u} - w^{n} - w^{v}) - r^{\varphi}; \\ w \text{=} \longleftarrow (w^{n}, w^{u}, w^{v}, w^{\varphi})^{T}; \end{array}
11:
                                                                                                                                                                                                                                                                                             Solve for Potential
12:
13:
               return w
14: end procedure
```

6. Error estimates, stopping criteria, and practical details

At each time step, a hierarchy of iterative numerical methods is applied, with each method requiring adequate stopping criteria and returning approximations to exact solutions. First, Newton's method returns the approximate solution to the nonlinear algebraic system. Second, at each Newton's iteration, the iterative solver PGMRES returns an approximate solution to the linearized residual function. Third, each Krylov iteration within PGMRES requires the application of the preconditioner. Finally, application of the preconditioner itself requires the solution of several linear systems.

In this work, we follow best practices used by the suite of solvers SUNDIALS [45] and implement computationally efficient strategies that ensure the nominal convergence rates of the global (time) integration error associated with a q-step BDF method, while minimizing computational costs due to Newton's and Krylov iterations.

We begin by defining the weighted norm of vector z as follows

$$||z||^{\circ} = \left[N^{-1} \sum_{i=1}^{N} (z_i/\mathbb{W}_i)^2 \right]^{1/2}, \tag{100}$$

where N is the number of vector elements and

$$W_i(y) = \text{RTOL}|y_i| + \text{ATOL}_i \tag{101}$$

are weights based on vector y and user-defined scalar relative tolerance RTOL and absolute tolerance vector ATOL_i. If $||z||^{\circ} \le 1$, the vector is *small* in the sense of the weighted norm above.

Newton's method seeks to find x such that F(x) = 0 iteratively. We stop after completing iteration $k \ge 1$ if the weighted norm of the update $\delta x^k = x^k - x^{k-1}$ is sufficiently small

$$R_k ||\delta x^k||^{\circ} \le \text{tol}_1 ||x^k - x^0||^{\circ},$$
 (102)

where

$$R_k = \max\{0.3R_{k-1}, ||\delta x^k||^{\circ}/||\delta x^{k-1}||^{\circ}\}, \quad k \ge 2,$$
(103)

is a coefficient updated after each Newton iteration (it is initialized to $R_1 = 1$), x^0 is the initial guess, and tol₁ is a fixed tolerance. The choice of x^0 and tol₁ require further explanation provided in Section 6.1.

The iterative solver PGMRES seeks to find a solution δx^k such that

$$I^{k-1}\delta x^k + F(x^{k-1}) = 0. {104}$$

Because a left preconditioner P is employed, we stop after completing Krylov iteration $m \ge 1$ if the ℓ^2 -norm of the preconditioned residual vector of the linear system is sufficiently small

$$||P^{-1}[J^{k-1}\delta x_m^k + F(x^{k-1})]||_2 \le \operatorname{tol}_2 ||P^{-1}F(x^{k-1})||_2, \tag{105}$$

where $\delta x_0^k = 0$ and tol₂ is a user-defined tolerance. We let tol₂ = 0.01, lower than that in Ref. [45].

The above stopping criterion yields the so-called *inexact* Newton's method, since the norm of the residual vector of the linear system is minimized relative to the norm of the Newton residual at the current Newton iteration. Both the residual vector and the Newton residual are used in their preconditioned form.

6.1. Initial guess, error estimates, and adaptive Newton tolerance settings

Recall that the solution to the nonlinear system of algebraic equations is the approximate solution to the system of ordinary differential equations at time step t_n . Even if the solution to the nonlinear system were exact, the truncation error associated with the fixed-leading coefficient form of the time integration BDF method remains. Thus, it is sensible to halt Newton's iterations when the error due to the finite number of iterations drops below a fraction of the temporal truncation error. Such strategy requires suitable estimates of the *leading truncation error* (LTE) associated with the BDF method [45] and of the error in Newton's latest iterate and is widely used in robust implementations of implicit time integration methods. For the sake of brevity, the implementation is summarized here, while the interested reader is referred to Ref. [45] for an in-depth discussion of guiding principles and practical approaches.

The current solution and the solution history at previous steps can be used to extrapolate in time with the same order of accuracy q using

$$x^* = \sum_{j=1}^{q+1} \beta_j^n x^{n-j},\tag{106}$$

where x^* is an extrapolation of order q, and the coefficients β_j^n are functions of the step size ratios h_j/h_{j-1} . The solution at t_n and its extrapolation provide the estimate

$$LTE = C(x_n - x^*), \tag{107}$$

where C is a coefficient that is a function of the order q and the time step ratios. To maintain the order of convergence of the BDF method globally while keeping the number of Newton iterations at a minimum, we stop when the Newton update is small compared to the LTE. That is

$$\frac{R_k||\delta x^k||^{\circ}}{C||x^k - x^{\star}||^{\circ}} < \text{tol}_1,\tag{108}$$

and we let $tol_1 = 0.05$.

6.2. Selection of state q^{\bullet} and preconditioner updates

Application of the preconditioner requires the solution of several linear systems, whose matrix of coefficients depend on state q^{\bullet} . The most obvious choice is to let q^{\bullet} be equal to the iterate q^{k-1} at Newton iteration k. While this approach guarantees that the preconditioner is always as close as possible to the Jacobian, it is computationally expensive. If the sequential linear systems within the preconditioner step are solved with direct methods, multiple factorizations need to be performed at each Newton's iteration. Similarly, if those linear systems are solved with iterative methods, their preconditioners will require updates. An alternative and popular strategy is to *freeze* the preconditioner at state q^{\bullet} , accepting the risk of compromising the rate of convergence of PGMRES in exchange for reduced computational costs.

In this work, the preconditioner is assembled once during the first Newton iteration and left unchanged during subsequent iterations. Consistent with the stopping criteria employed, this first iterate is set equal to the extrapolated solution as in Eq. (106). Furthermore, the opportunity of leaving the preconditioner unchanged over subsequent time steps was also explored. We conducted extensive testing on the convergence of PGMRES with frozen preconditioners and a detailed discussion of the results is presented in Section 7.

7. Applications

7.1. Implementation details and performance metrics

The Portable, Extensible Toolkit for Scientific Computation (PETSc) was used as a framework for the Message Passing Interface (MPI) parallelization of the PDE solver [47,48]. PETSc is a library for large-scale numerical computations that offers

a variety of matrix assembly and discretization tools, preconditioners, linear and nonlinear solvers, and time-integrators for ordinary differential equations that facilitated greatly the implementation of the numerical method presented here.

A brief overview of the metrics relevant to the JFNK solver is provided in this section as well, which will help assess the performance of the solver in later sections. At the top of the hierarchy, the performance of the nonlinear solver is assessed by monitoring the number of nonlinear iterations required for convergence. For each Newton iteration, the "outer" linear system arising from the monolithic implicit method is solved by an iterative Krylov method. Five additional "inner" linear systems are solved for each outer Krylov iteration in order to apply the preconditioner. These five linear systems are associated with matrices P_n , P_u , P_v , Q, and P_{φ} . Attention is placed primarily on the 4 systems arising from spatial operators and numerical boundary conditions (P_n , P_u , P_v , and P_{φ}), since matrix Q is easily inverted by direct solvers applied to the independent 3×3 blocks on its diagonal. For simplicity, we denote the number of outer GMRES iterations as GMRES_o, the sum of inner GMRES iterations as GMRES_i, and the number of inner GMRES iterations required for the solution of the electron preconditioning matrix P_n as GMRES_o.

The linear systems involved in preconditioning the number densities of electrons and ions, i.e. those with matrices P_n , P_u , P_v , are preconditioned with factors from ILU decomposition to level 1 obtained with the HYPRE euclid algorithm [49] available in PETSc. The system associated with the Poisson equation for the electric potential due to the space charge, i.e. that associated with P_{φ} , is solved using a direct LU decomposition performed once by the MUMPS package [50,51], also available in PETSc.

7.2. Parallel plates streamer discharge

7.2.1. Configuration, parameters, and discretization

The performance of our novel integration and preconditioning strategy is assessed first by simulating the propagation of a streamer between two parallel electrode plates. Streamer propagation between parallel plates is a simple configuration that allows for the study of streamers, it is used for comparison and validation of plasma solvers [32], and to study the effect of select processes [52] and test numerical methods [53].

Two parallel circular plates are placed at a distance H and the domain extends a distance of R in the radial direction. A constant voltage is applied at the driven top electrode, generating an electric field that is below breakdown. A seed of positive charge is placed in between the electrodes to enhance the electric field locally. This seed distribution leads to the formation and propagation of a streamer.

We consider air at 300 K and 1 atm. The simulation is initialized with uniform number densities of positive ions and negative charges equal to $10^{15}~{\rm m}^{-3}$. Electrons account for 99% of negative charges and negative ions for the remaining 1%. A constant applied potential $\tilde{\phi}_{\rm app}$ induces a constant background electric field of 15 kV cm⁻¹. A kernel of positive ions with a Gaussian spatial distribution is placed in between the parallel plates

$$\tilde{u} = \tilde{u}_0 \exp\left[-\frac{\tilde{r}^2 + (\tilde{z} - \tilde{z}_0)^2}{\tilde{\sigma}^2}\right],\tag{109}$$

where $\tilde{u}_0 = 5.0 \times 10^{18} \text{ m}^{-3}$, $\tilde{z}_0 = 0.6\tilde{H}$, and $\tilde{\sigma} = 0.35 \text{ mm}$. The kernel induces a local enhancement in the electric field above breakdown. A schematic of the configuration is shown in Fig. 2.

Second order centered finite-difference operators are used to approximate the gradient and Laplacian operators. The domain is discretized on a Cartesian mesh with constant spacing in the axial direction of approximately 1.2 μ m and 4200 points. The minimum spacing in the radial direction is 0.3 μ m, stretched with a constant factor of 1.01 using 500 points. Overall, the mesh consists of 2.1 million grid points, resulting in a system of 8.4 million unknowns. Simulations are conducted using first, second, and third order BDF methods, and the effect of the order of temporal accuracy is discussed later. The boundary conditions are applied as described in Section 2.2, and are summarized in Table 1. The parameters of the parallel plates configuration are summarized in Table 2.

7.2.2. Discharge overview

The kernel of positive ions induces a local 200-300 Td reduced electric field, which leads to high values of ionization rate. Ionization leads to the rapid growth of electron number densities, which combined with electric drift, leads to the accumulation of space charge at the front of a developing streamer. After 4 ns, the number densities at the front approach 10^{20} m⁻³ sustaining a self-propagating streamer that induces a local electric field of 600 Td. The overall evolution of the electric field is shown in Fig. 3. In Fig. 4, one dimensional profiles of the electron number density are shown, along with the electric field magnitude on the axis. The emission of electrons at the cathode is low and the initial layer at the cathode grows in the direction of the anode. The insets provide a close up view of the anode sheath, where large gradients of the number density are apparent. However, the number densities of the charged species remain low and there is no space-charge effects on the electric field inside the sheath. Overall, the values of the number densities and electric field at the front of the self-propagating streamer are representative of those in a gap streamer discharges between pins [54–56].

7.2.3. Convergence

From a computational perspective, it is desirable to integrate the system of equations with the highest temporal order possible that produces a stable numerical solution. The JFNK framework is hierarchical and requires appropriate tolerances

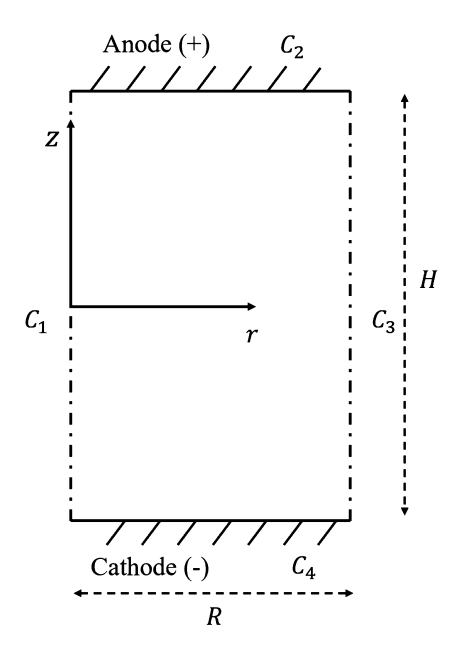


Fig. 2. Overview of the computational domain for the parallel plates streamer discharge presented in Section 7.2.

Table 1 Boundary conditions for the parallel plates streamer discharge in Section 7.2. For any variable x, ∂_y indicates $\nabla x \cdot \boldsymbol{e_y}$, i.e. the projection of the gradient onto the unit vector of coordinate y. ζ is the coordinate introduced in Section 2.2. θ_{ζ} is the component of the electric field in the ζ direction.

Boundary Conditions, parallel plates				
-	n	и	ν	φ
C ₁	$\partial_r n = 0$	$\partial_r u = 0$	$\partial_r v = 0$	$\partial_r \varphi = 0$
C_2	$a_2T_e\partial_z n + Vn = 0$	$a_8\partial_z u + Vu = 0$	$a_8 \partial_z v + V v = 0$	$\varphi = 0$
C_3	$\partial_r n = 0$	$\partial_r u = 0$	$\partial_r v = 0$	$\partial_r \varphi = 0$
C_4	$-a_2T_e\partial_z n + Vn = \chi$	$-a_8\partial_z u+Vu=0$	$-a_8\partial_z v + V v = 0$	$\varphi = 0$
V	$c_{\text{mxw}}/2 + a_1 \theta_{\zeta}$	$ w_u -a_7\theta_\zeta$	$ w_v + a_7 \theta_\zeta$	N/A

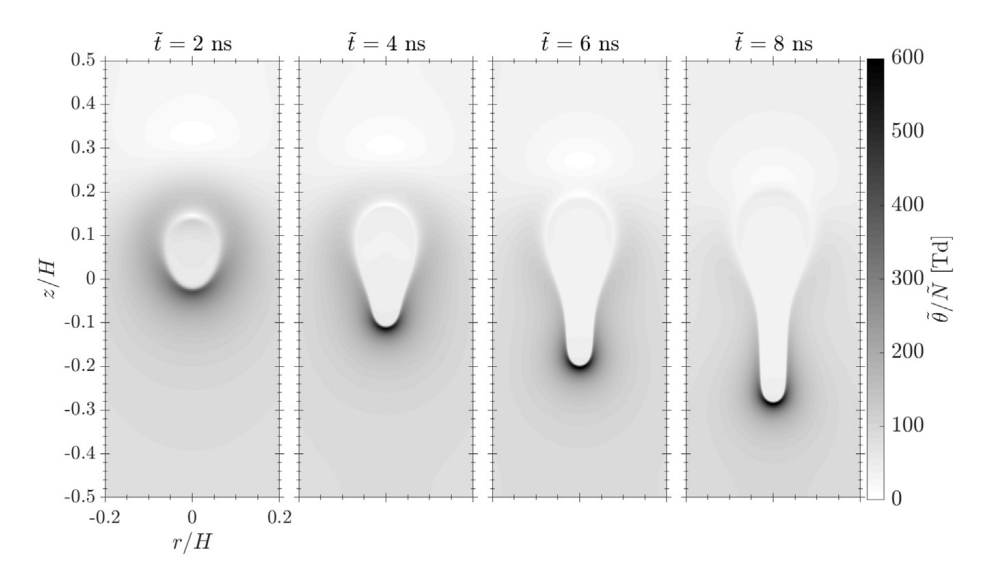


Fig. 3. Snapshots of the reduced electric field strength at 4 instants in time, showing the formation and propagation of the streamer.

Table 2Configuration parameters for the parallel plates discharge in Section 7.2.

tion 7.2.					
Geometry and Discharge					
0.5 cm					
0.25 cm					
1.2 μm					
0.3 μm					
2.1 M					
7.5 kV					
$10^7\ m^{-3}\ s^{-1}$					
Gas Properties					
300 K					
1 atm					
Boundary Conditions					
0.001					
strong-field					
Reference Values					
10.35 Td					
0.1114 ns					
$10^{18}\ m^{-3}$					
14.00 μm					
$4.118\times10^4\text{K}$					

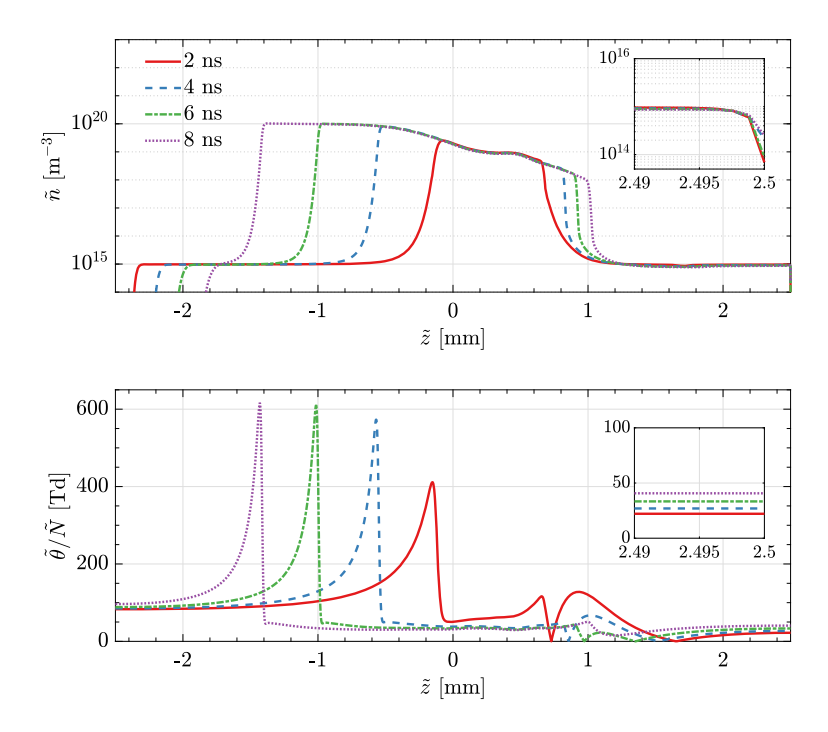


Fig. 4. One dimensional profiles of the electron number density and reduced electric field for the parallel plates discharge, taken along the axis of symmetry at various instants in time. Detailed views of the anode sheath are provided in the insets.

for all linear and nonlinear solvers, so that it is critical to ensure that the observed order of temporal convergence matches the theoretical one. To this end, a set of solutions were computed with time steps in the range 10 to 30 ps with BDF methods of order 1, 2, and 3. The solutions were then compared against an "exact" solution computed with a small time step size equal to 3 ps and the constant step size BDF method of order 3. The results of this convergence study are shown in Fig. 5.

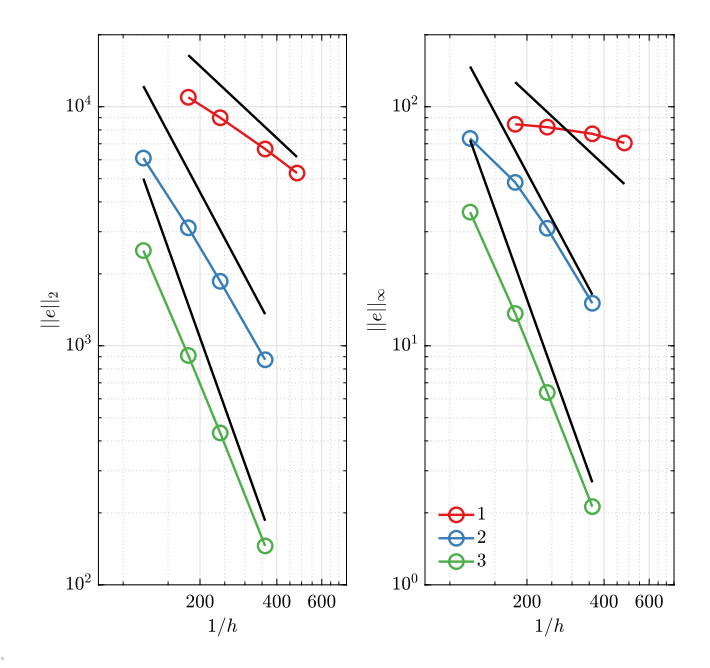


Fig. 5. Vector norms of the error at t = 4 ns for the solution vector including n, u, and v as a function of the time step size for BDF methods of order 1, 2, and 3. The nominal convergence rates of the error are shown as solid black lines. (For interpretation of the colors in the figure(s), the reader is referred to the web version of this article.)

The error convergence (measured using both the ℓ_2 -norm $||e||_2$ and ℓ -infinity norm $||e||_\infty$) using second and third order BDF methods is observed to match the theoretical rate of convergence closely as shown in Fig. 5. The rate of error convergence observed with BDF 1 is lower than the theoretical one, especially in the infinity norm. It is emphasized that the error norm is dominated by errors in the region surrounding the streamer front, where the number densities are largest. Less accurate solutions were found to overestimate the streamer velocity and if the solution is very inaccurate, the location of the front of the streamer will not match that of the exact solution. This might explain the slow convergence rate of BDF 1 and why the infinity norm does not follow the expected asymptotic behavior over the range of time step sizes considered. Even for time steps that are outside the region of asymptotic convergence, it is clear that higher order methods provide a significant advantage in terms of accuracy for the same time step size as expected. The remainder of this work uses BDF methods with orders of 2 and 3, unless otherwise stated.

The same streamer discharge in between parallel plates is also used to characterize the convergence of the electrostatic potential and number density of charges with respect to a refinement in the finite difference grid. Convergence is assessed by refining in the axial direction and the error is computed with respect to the solution with the most spatial resolution. All solutions on finite difference meshes of varying resolution are obtained by taking 20 steps with the same time step size. Solutions are then compared at approximately 0.2 ns from the initial condition.

Fig. 6 shows the 2-norm error for the electrostatic potential and for the number density of charged particles as a function of the inverse of the grid spacing in the axial direction. It is apparent that a second-order rate of convergence is recovered, consistent with the order of the centered finite difference approximations to differential operators in space, i.e. gradient and Laplacian.

7.2.4. Performance assessment

In order to assess the performance of our novel preconditioner, we consider metrics that describe the efficacy of the preconditioner and the computational costs associated with its application. Overall, there are several competing factors to consider. The number of time steps per factorization f is an important parameter, because computing the factorizations required during the application of the preconditioner accounts for most of the computational cost. However, the savings that ensue from reusing factors may be negated by the additional Krylov iterations required for convergence at each Newton step when the preconditioner becomes stale. Larger time steps h require fewer steps for a fixed time interval, but smaller time steps might be less expensive for the JFNK and more amenable to reusing factorizations. In what follows, we present and discuss several performance metrics that were introduced and defined in Section 5.

We begin by examining the number of Newton iterations and $GMRES_0$. In Fig. 7 the temporal evolution of the number of Newton iterations per time step, and $GMRES_0$ per Newton iteration for varying h and f are presented. The number of Newton iterations remains bounded between 2 and 4 iterations at all times. The evolution of $GMRES_0$ illustrates that the linearized residuals are easier to solve during the first few nanoseconds, when the streamer has not developed fully and the gradients of the number density are low. During this early stage of the discharge, reusing the factors involved in the application of the preconditioner has very little impact on $GMRES_0$. As the electric field ahead of the streamer increases

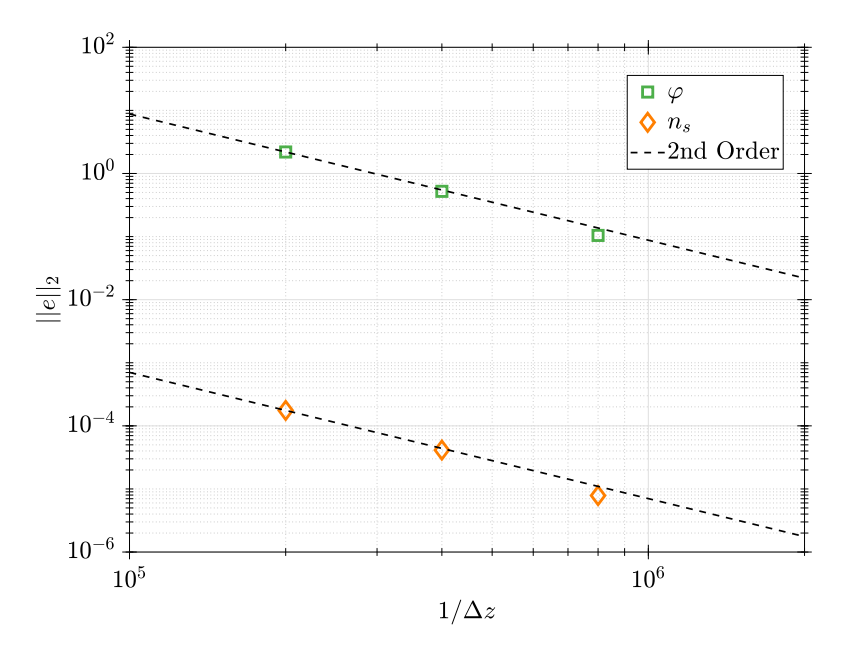


Fig. 6. Convergence of the electrostatic field and number density of charges at 0.2 ns, corresponding to 20 steps from the initial conditions. The error is computed with respect to a solution on the finest mesh with $0.6 \mu m$ resolution.

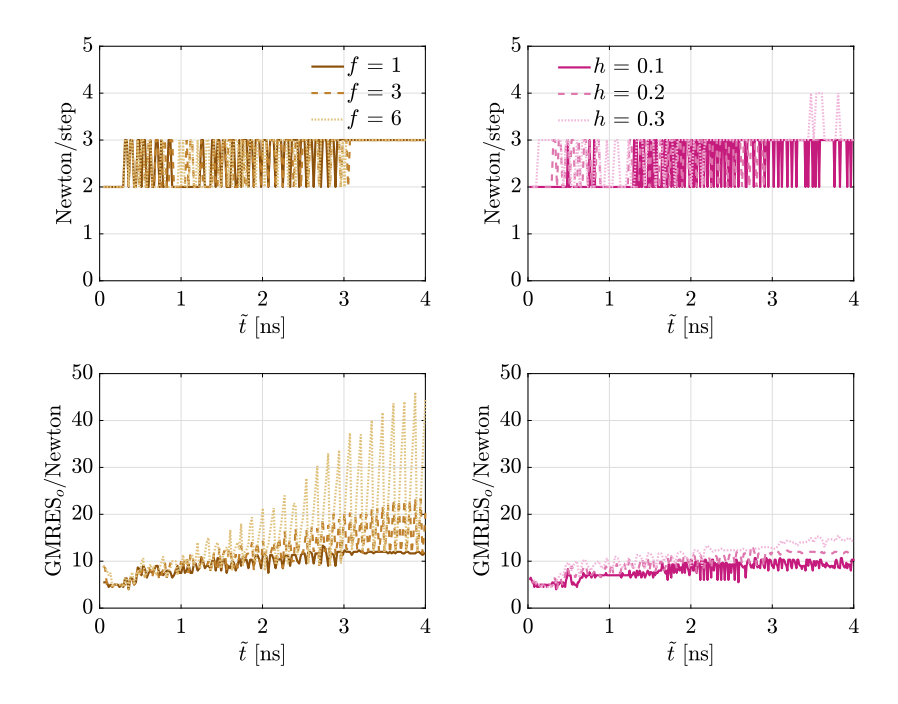


Fig. 7. Newton iterations per time step (top row), and GMRES iteration per Newton iteration (bottom row) with BDF 2. In the left column, constant time step sizes h = 0.2 are taken, while in the right column matrix factors are recomputed at every time step and not reused.

along with the number densities of charges, the problem becomes considerably more stiff, at which point the savings from larger time steps and fewer factorizations are offset by a greater number of linear iterations required for convergence.

Averaged performance metrics up to 4 ns without reusing factors are presented in Table 3. There is a modest dependence on the order of the BDF method, while the time step size has a more significant impact on the number of linear iterations required for convergence, with larger time steps resulting in a greater number of iterations as expected. It is important to emphasize that about 85% of GMRES_i consists of iterations required to apply the electron number density preconditioner. This is an important and encouraging finding since it suggests the opportunity to use more affordable approximate techniques to solve the systems associated with the number densities of ions, as opposed to the ILU method employed in this work. This bodes well for the extension towards plasma models that involve many ions also.

In Fig. 8, the wall-clock time per step (measured in minutes) and the overall wall-clock time are compared for different time step size with BDF of order 2. The data are shown as a function of the product of the time step h and the number

Table 3 Performance statistics for simulations conducted with BDF 2 and BDF 3, and dimensionless time steps varying from 0.1 to 0.3, corresponding to 10 to 30 ps in physical time. Matrix factorizations were not reused (f=1).

BDF	h	Newton step	GMRES _o Newton	GMRES _o	GMRES ₀
2	0.1	2.51	8.42	27.9	23.6
2	0.2	2.67	10.7	43.79	38.9
2	0.3	2.84	13.2	56.8	51.9
3	0.1	2.00	8.32	24.2	20.0
3	0.2	2.69	9.70	37.4	32.8
3	0.3	2.86	11.6	49.5	44.7

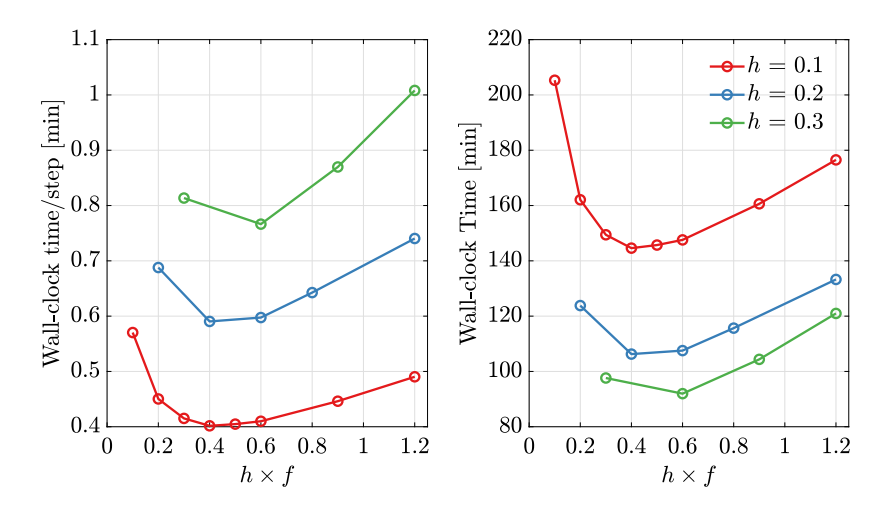


Fig. 8. Wall-clock time/step vs. $h \times f$ (left) and total wall-clock time vs. $h \times f$ for a BDF order 2. Equal values on the *x*-axis indicate an equal number of factorizations per physical time for all cases.

of steps per factorization. The objective is to account for the aforementioned competing effects related to taking large time steps and to the reuse of matrix factorizations. In this respect, the product $h \times f$ represents the inverse of the frequency (in physical time) at which the factors are recomputed. The measurement of the wall-clock time per step shows that smaller time steps ease the task for the iterative linear solver, but such a positive improvement does not scale linearly, as shown by the overall wall-clock time required to advance the solution to 4 ns. Smaller time steps imply a more costly simulation overall, although as expected, it is easier to offset such cost through the reuse of factorizations when compared to larger time steps. In the range of time step sizes explored, reusing the factorization for 2 to 4 consecutive steps appears to be a reliable manner of reducing the overall wall-clock time.

Fig. 8 suggests that $h \times f$ equal to 0.6 for h = 0.3 is optimal, which translates to about ~ 15 factorizations per nanosecond during streamer propagation with time steps of size equal to 0.3 ns. This information can be leveraged to obtain a cost estimate for a given gap distance and streamer velocity. It is emphasized that such performance analysis and related conclusions are specific to the current implementation of the solver with PETSc, which is remarkably flexible, albeit most likely not optimal at this point.

7.3. Axisymmetric pin-to-pin streamer discharge

In this Section, we explore the simulation of streamer ignition and propagation in an axisymmetric pin-to-pin configuration at atmospheric conditions. The curvature of the pin tip is the characteristic geometric feature that determines a local enhancement to the electric field. Paraboloids provide a simple geometry uniquely characterized by the tip curvature, making them convenient and realistic approximations to pin electrodes [55,57]. The geometry of the configuration is depicted schematically in Fig. 9. Two axially oriented parabolic pins with a radius of curvature r_c at the tip are separated by a gap of length H, where the anode (driven electrode) is at the top, and the cathode (grounded electrode) at the bottom. The two electrode surfaces are bounded by a circular arc of radius R, which forms the far-field boundary. At the base, the pin has radius equal to \overline{r} , and $\overline{\theta}$ is the angle formed between the axis r and the segment connecting the origin to the pin base at radial location \overline{r} .

A time-varying voltage is applied according to the sigmoid profile

$$\phi(t) = \phi_{max} \left[\sigma(t - \delta, \lambda) + \sigma(t - \delta - t_p - t_r, -\lambda) - 1 \right], \tag{110}$$

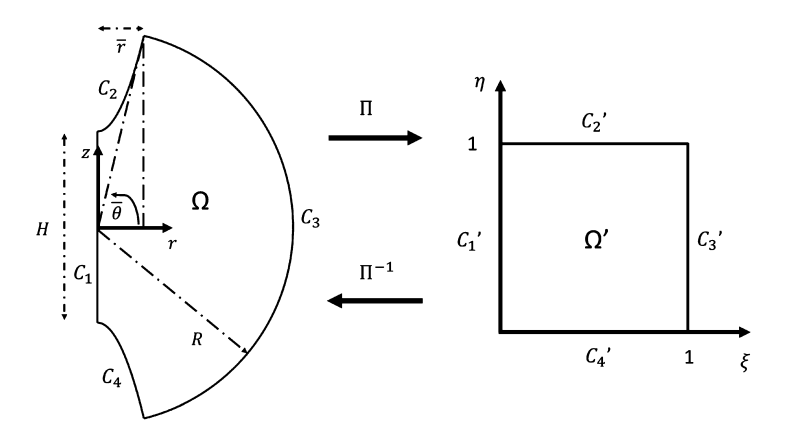


Fig. 9. Geometrical domain and corresponding computational domain using a curvilinear transformation as in Section 7.3.

$$\sigma(t,\lambda) = 1/(1 + \exp(-\lambda t)). \tag{111}$$

Compared with the previous test case, this configuration introduces significant complexity, as the sharp electrode tips increase the nominal electric field locally by a factor of 5.2. Additionally, as it will be shown, plasma streamers form near and propagate away from the electrode tips, introducing numerical challenges related to the nonlinearity of the numerical boundary conditions. The simulation is limited to the ignition and streamer propagation phases until connection.

7.3.1. Configuration, parameters, and discretization

A body-fitted curvilinear grid [58] is generated to fit the boundaries of the computational domain and transformations Π and Π^{-1} are employed to map to and from Cartesian and curvilinear coordinate systems. An overview of the configuration is shown in Fig. 9 with important geometrical parameters and boundaries surfaces labeled C_1 through C_4 . The surfaces in the physical domain are mapped to surfaces C_1' through C_4' in the transformed domain.

The transformation Π results in a mapping of the left boundary

$$C_1: r = r(\xi, \eta) = 0,$$
 (112)

$$z = z(\xi, \eta) = -0.5 + \eta,$$
 (113)

top boundary

$$C_2: r = r(\xi, \eta) = \xi \overline{r},\tag{114}$$

$$z = z(\xi, \eta) = \kappa \overline{r}^2 \xi^2 + 0.5,$$
 (115)

right boundary

$$C_3: r = r(\xi, \eta) = R\cos(-\overline{\theta} + 2\overline{\theta}\eta), \tag{116}$$

$$z = z(\xi, \eta) = R\sin(-\overline{\theta} + 2\overline{\theta}\eta),\tag{117}$$

and bottom boundary

$$C_4: r = r(\xi, \eta) = \xi \overline{r},\tag{118}$$

$$z = z(\xi, \eta) = -\kappa \bar{r}^2 \xi^2 - 0.5,$$
 (119)

where $\kappa = 1/(2r_c)$. The curvilinear mesh is computed following the procedure outlined in Ref. [58]. The Laplacian and gradient operators, and expressions for the normal derivatives are linear combinations of derivatives in ξ and η . These are determined through the known mapping between the physical and computational domains and details are provided in the Appendix. Boundary conditions are summarized in Table 4.

Pin electrodes with radius of curvature of 150 μ m and gap of 2.5 mm are selected. The initial condition consists of a constant number density of positive ions equal to 10^{15} m³ balanced by an equal number density of negative particles consisting of negative ions (95%) and electrons (5%).

The domain extends approximately 3 gap lengths axially and 1.5 gap lengths radially. The background gas is atmospheric air at 300 K. Centered second-order finite difference operators are used for all derivatives, which match the order of the operators used to generate the curvilinear meshes and for the transformed derivatives. All parameters are summarized in Table 5.

Table 4 Boundary conditions for the pin-to-pin discharge in Section 7.3. For any variable x, ∂_y indicates $\nabla x \cdot \boldsymbol{e}_y$, the projection of the gradient onto the unit vector of coordinate y. N represents the direction normal to the boundary, and ζ is the coordinate defined in Section 2.2. θ_{ζ} is the component of the electric field in the ζ direction.

Boundary Conditions, pin-to-pin					
-	n	u	v	φ	
<i>C</i> ₁	$\partial_N n = 0$	$\partial_N u = 0$	$\partial_N v = 0$	$\partial_N \varphi = 0$	
C_2	$a_2 T_e \partial_{\zeta} n + V n = \chi$	$a_8 \partial_{\zeta} u + V u = 0$	$a_8 \partial_\zeta v + V v = 0$	$\varphi = 0$	
C_3	$\partial_N n = 0$	$\partial_N u = 0$	$\partial_N v = 0$	$\partial_N \varphi = 0$	
C_4	$a_2 T_e \partial_{\zeta} n + V n = \chi$	$a_8\partial_\zeta u+Vu=0$	$a_8 \partial_\zeta v + V v = 0$	$\varphi = 0$	
V	$c_{ m mxw}/2 + a_1 \theta_{\zeta}$	$ w_u -a_7\theta_\zeta$	$ w_{\nu} + a_7 \theta_{\zeta}$	N/A	

Table 5Configuration parameters for the pin-to-pin discharge in Section 7.3.

Geometry a	Geometry and Discharge					
$ ilde{H}$	0.25 cm					
\tilde{r}_c	150 μm					
Ŝ	$10^7 \mathrm{m}^{-3} \mathrm{s}^{-1}$					
Pulse Param	Pulse Parameters					
$ ilde{\phi}_{ ext{max}}$	12.5 kV					
\tilde{t}_p	0.1 ns					
\tilde{t}_r	5 ns					
$ ilde{\delta}$	3.2 ns					
$ ilde{\phi}_{ ext{max}} \ ilde{t}_p \ ilde{\delta} \ ilde{\delta} \ ilde{\lambda}$	$8/\tilde{t}_r$					
Gas Propert	Gas Properties					
\tilde{T}_B	300 K					
\tilde{P}_B	1 atm					
Boundary C	Boundary Conditions					
n _{em}	0					
γ	0.001					
ion BCs	strong-field					
Reference Values						
$\tilde{ heta}_0$	10.35 Td					
\tilde{t}_0						
\tilde{n}_0	$10^{18} \ \mathrm{m}^{-3}$					
$ ilde{\lambda}_0$	14.00 μm					
\tilde{T}_{0}	$4.118 \times 10^4 \text{ K}$					

7.3.2. Discharge overview

The equations are discretized on 3 meshes consisting of 1.05 M, 2.1 M, and 4.20 M grid points. The time step size is selected through an adaptive strategy implemented in PETSc based on the Local Truncation Error (LTE) to satisfy user-specified tolerances. In this work, a relative tolerance of 10^{-3} is used, and absolute tolerances of 10^{12} m⁻³ for charged species and 10^{-6} V for the induced potential are utilized. The adaptive strategy ensures that the time step size changes in response to the LTE estimate, but time steps that do not fall below the specified error tolerances are not rejected in order to reduce computational costs. A maximum dimensionless time step of 0.4 corresponding to approximately 45 ps and a BDF method of order 3 are used unless otherwise noted.

An overview of the discharge is shown in Fig. 10. At the curved electrode tips, the electric field is higher by a factor of 5.2 compared to the nominal electric field, defined as the ratio of the bias voltage to the electrode gap distance. The increase in the applied voltage leads to elevated electric fields near the tips and intense ionization. Eventually, electron avalanches lead to the formation of a cathode-directed positive streamer at the anode (top electrode) and an anode-directed negative streamer at the cathode (bottom electrode). While the two streamers are similar in structure, the positive streamer has a smaller radius, higher number densities at its front, and higher induced electric fields compared to the negative streamer. In Fig. 11, one-dimensional profiles of the number densities of electrons, positive ions, and negative ions at the axis of symmetry are plotted along with the magnitude of the reduced electric field strength.

The small offset between positive ions and electrons results in a thin positive charge at the head of the cathode-directed streamer, and a negative charge layer at the head of the anode-directed streamer. The number densities of the negative ions increase rapidly behind the streamer head, with maximum values roughly two orders of magnitude lower than electrons and positive ions. Number densities and reduced electric field magnitude are consistent with those observed in other streamer

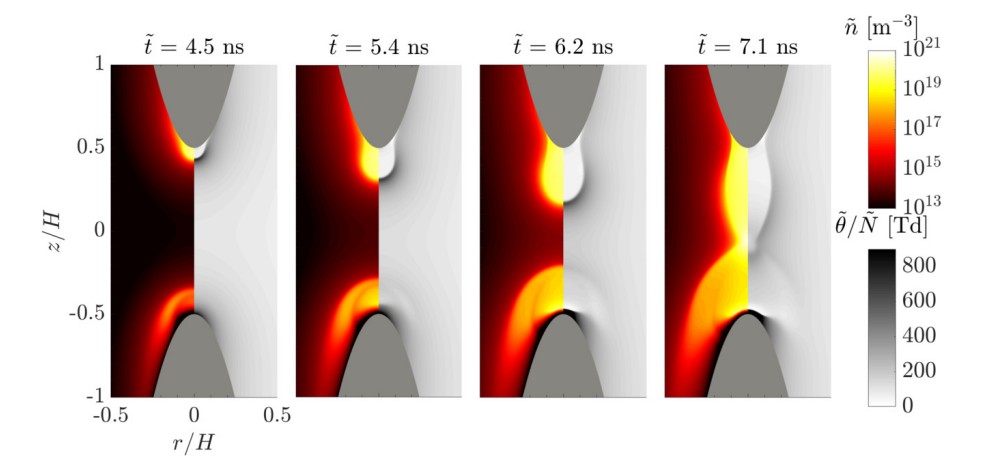


Fig. 10. Electron number density (left panels) and magnitude of the reduced electric field (right panels) at 4 instants in time during streamer propagation.

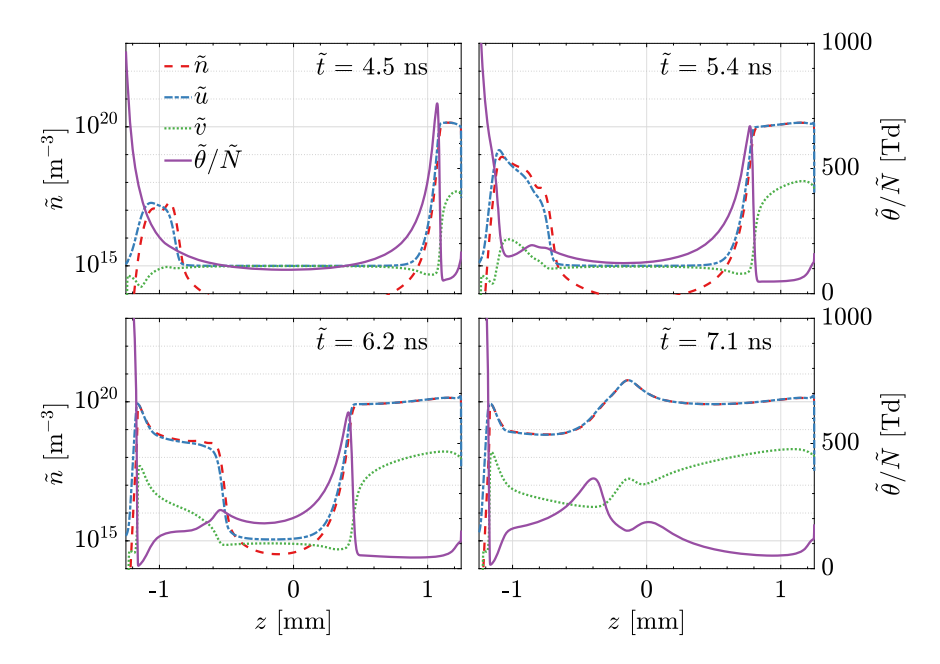


Fig. 11. One-dimensional profiles of number densities of the charged species and the reduced electric field strength in axisymmetric pin-to-pin discharges, taken along the axis and various instants in time.

discharges in the glow regime of Nanosecond Pulsed Discharges [55,56]. There is also remarkable similarity between this positive streamer and that propagating between circular parallel plates discussed in Section 7.2 (see Fig. 4), with reduced electric field around 600 Td and peak number densities around 10^{20} m⁻³.

For the axisymmetric pin-to-pin discharge, one-dimensional profiles show a distinctive feature near the cathode where there is a lack of negative charges and a very large electric field, a region commonly known as cathode sheath [14]. As opposed to the parallel plates discharge, the number densities near the anode are large enough to change the applied reduced electric field appreciably. Naturally, this produces a tighter coupling between the charged species and the electrostatic potential near the anode.

7.3.3. Performance assessment

The performance of the JFNK solver for pin-to-pin gap discharges is assessed using the same approach as for the parallel plates discharge case. Fig. 12 shows the time step size history and relevant statistics as a function of time. At the onset, prior to ignition, number densities are low and the solver is able to maintain the desired accuracy while taking the largest admissible time step size of 45 ps with a low number of Newton and GMRES₀ iterations. This early period is followed by the time step size changing rapidly in response to the increasing electric field and its subsequent decrease due to shielding by the space charge at the anode before streamer ignition (denoted by a dashed vertical line in Fig. 12). After ignition, the time step size continues to decrease until it reaches a plateau around 25 ps during streamer propagation. Finally, the time step size decreases due to the rapidly evolving electric field between the two approaching streamers that precedes the formation of a conducting plasma channel.

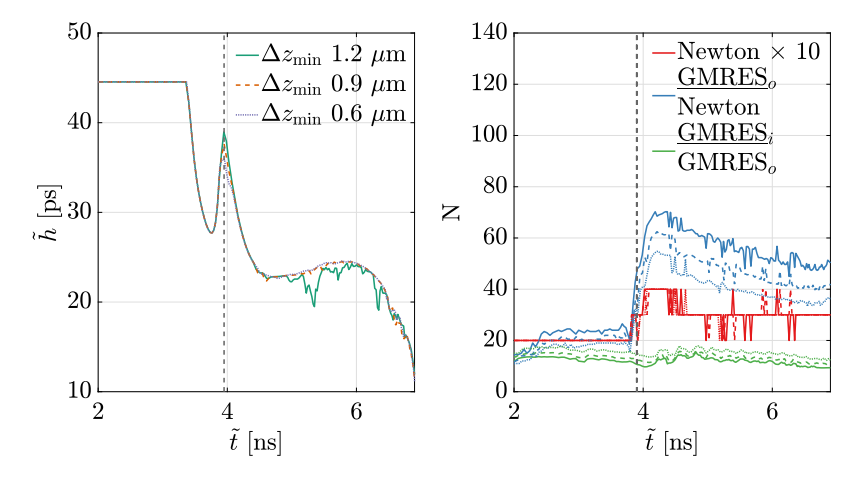


Fig. 12. Time step history (left) and statistics for Newton, GMRES/Newton, and inner per outer GMRES iterations (right) as a function of time for three different resolutions (line styles are the same as in the left figure). The vertical dashed line represents streamer ignition.

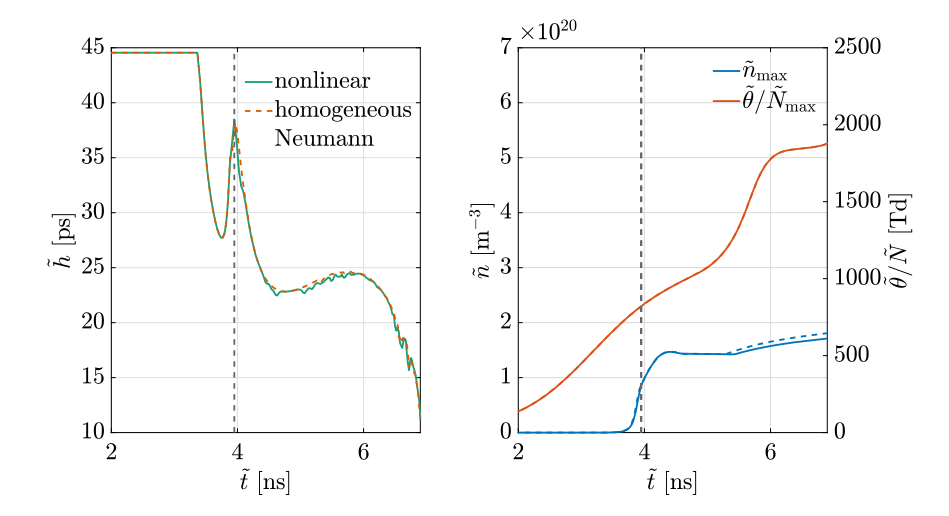


Fig. 13. Time step size history (left), and maximum values of the electron number density and reduced electric field (right) comparing nonlinear boundary conditions in Section 2.2 (solid) and homogeneous Neumann conditions at the anode (dashed).

The number of Newton iterations per step falls between 1 and 4 throughout the simulation. The GMRES₀ metric at the onset of the simulation is similar to that observed for the parallel plates case with GMRES₀/Newton between 10 and 30. However, streamer ignition marks a significant departure for the ratio GMRES₀/Newton, which increases quickly to a value in the range of 40 to 70. This happens despite the fact that the electric field strengths and number densities at the streamer head are very similar to those encountered in the parallel plates discharge. Despite this commonality, the number densities and electric field strengths near the electrodes are much higher for the axisymmetric pin-to-pin discharge, which makes attaining convergence at each Newton iteration more challenging.

It is also observed that spatial resolution has a modest effect on the performance of the solver. An increase in spatial resolution has a negligible effect on the history of time step sizes, which is a likely indication that the spatial resolution is adequate. This behavior is in contrast with the marked effect of resolution on GMRES₀ metrics, which indicates that an increase in spatial resolution improves convergence, probably due to discretization and numerical (not physical) effects.

An additional numerical experiment was carried out to analyze the effect of boundary conditions on computational costs. The simulation of the pin-to-pin discharge is repeated with a modification to the boundary conditions at the anode (top electrode), which are changed to homogeneous Neumann for all charged species. The original nonlinear boundary conditions presented in Section 2.2 are left unchanged at the cathode (bottom electrode), ensuring the formation of the cathode sheath. The time step size history and the maximum values of the reduced electric field and electron number densities are shown in Fig. 13 for the simulation using the medium resolution mesh.

The discharge physics simulated with the original nonlinear boundary conditions are recovered almost exactly with simpler homogeneous Neumann conditions at the anode with the time step size history following the same behavior closely. These conclusions are strengthened by the observed temporal evolution of the maximum values of reduced electric field and electron number density, where the only difference is a slight overestimation of the maximum electron number density as

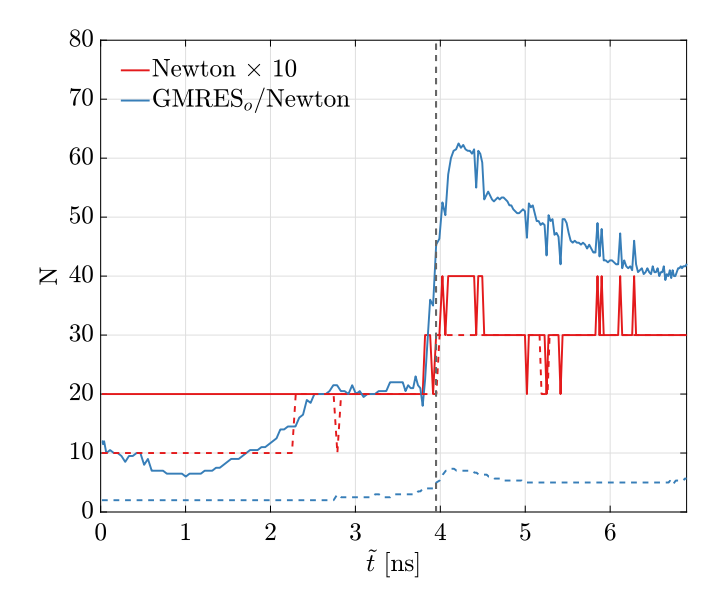


Fig. 14. Newton iterations \times 10 and GMRES₀/Newton as a function of time for the full nonlinear boundary condition (solid line) and the homogeneous Neumann conditions at the anode (dashed lines).

the streamer propagates. Two dimensional contour plots (not shown) are indistinguishable from those presented in Fig. 10, confirming the negligible effect of the sheath formed around the anode during the streamer ignition and propagation phases.

The assessment of the solver performance with these alternative boundary condition is presented in Fig. 14. The number of Newton iterations is not affected in any significant way by the new boundary condition, but the ratio GMRES₀/Newton is lower by a factor of 6, leading to substantial computational savings. We conclude that in the original approach, the majority of the Krylov iterations is spent to address the anode sheath, probably an unjustified expense considering its negligible impact on discharge dynamics. At the very least, we conclude that the linearization used in the proposed preconditioning framework is not quite effective for the anode sheath on the meshes explored in this study. However, the trends observed in Fig. 12 with respect to spatial resolution suggest that a spatial resolution close to 0.15 µm near the anode surface might induce performance similar to that observed with the modified anode boundary condition. Yet, this is not a feasible option considering the increase in problem size. It is also difficult to justify given the limited effect that additional resolution provides to the simulation of discharge physics, and a more sensible manner of proceeding might be to seek a different preconditioning strategy for the charge densities at the boundary points.

The important decrease in the number of outer iterations corresponds to a similar decrease in the overall wall-clock time, from 8.5 to 1.5 hours required to simulate the two streamers connecting across the electrode gap. This significant decrease in wall-clock time further emphasizes the need for improved preconditioning at the boundary or for alternative boundary conditions that allow for the simulation of accurate physical processes with high fidelity.

8. Computational resources and scaling

The simulations presented in Section 7 employed HYPRE ILU to precondition the linear systems associated with charged species, and MUMPS LU to precondition the linear system associated with the electrostatic potential. Such preconditioners based on incomplete and complete factorizations provided a robust implementation for the modest problem sizes and extent of parallelization. However, the performance of such preconditioning strategy deteriorates rapidly with increasing problem size and processor count. Below, we discuss the outcome of numerical tests that assess the performance of more scalable preconditioners readily available in PETSc. The results presented in this section demonstrate that our novel physics-based preconditioning strategy is scalable when paired with a number of widely used preconditioners for the inner linear systems. The discharge configuration presented in Section 7.2 was selected, while the boundary conditions for charged species were set to homogeneous Neumann on both electrodes. This approach lessens the effect of spatial resolution of the sheath on the number of linear iterations as observed in Fig. 11 and discussed in related commentary. The solver was allowed to take 10 steps of size h = 0.1 using BDF 2. Each step is about 10 ps in size. Such time step size was chosen for those tests as it is comparable to the size taken by solvers that use explicit time integration on rather coarse spatial discretizations, although much larger stable and accurate time steps are possible on the account of the high-order implicit BDF schemes implemented and their exceptional stability. Results using various preconditioners for charged species, and BoomerAMG for the potential are presented in Table 6 for problem sizes ranging from 1.2 M to 19.2 M grid points.

We observe that the number of Newton iterations remains nearly constant as the problem size increases alongside with the number of processors, while there is a moderate increase in the Krylov/Newton ratio. In general, we observe very good scaling in terms of wall-clock time per step (time/step) when compared to the corresponding ratio of stable time step size as it relates to CFL conditions. There is a noticeable decrease in performance for the finest grid, but it is still very favorable

Table 6Grid performance study using BDF 2 and h = 0.1 for 10 steps. Homogeneous Neumann conditions for charged species are used at both electrodes. All configurations used HYPRE BoomerAMG for the linear system associated with the potential. The preconditioners for charged species are Algebraic Multigrid (PETSc PCGAMG), Block Jacobi, and Generalized Additive Schwarz (PETSc PCGASM).

Grid	<u>h</u> h _{CFL—A}	<u>h</u> h _{CFL} D	CPUs	<u>Newton</u> step	GMRES _o Newton	time [s] step
AMG						
400 × 3000	2	1.1	56	2.0	2.1	17.9
800×6000	4	4.5	224	2.0	3.0	18.1
1200×9000	6	10.1	504	2.0	4.0	23.6
1600×12000	8	17.8	896	2.3	4.6	34.3
Block Jacobi						
400 × 3000	2	1.1	56	2.0	2.4	9.40
800×6000	4	4.5	224	2.0	3.2	9.35
1200×9000	6	10.1	504	2.0	3.9	12.7
1600×12000	8	17.8	896	2.4	4.6	19.9
Generalized Additive Schwarz						
400 × 3000	2	1.1	56	2.0	2.4	9.85
800×6000	4	4.5	224	2.0	3.3	9.87
1200×9000	6	10.1	504	2.0	3.9	12.9
1600×12000	8	17.8	896	2.2	4.4	19.6

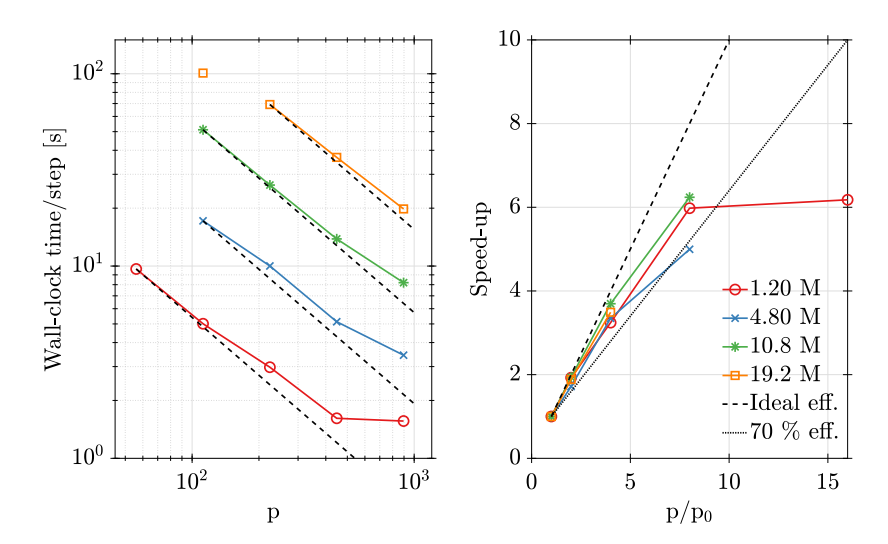


Fig. 15. Wall-clock time/step (left) and parallel speed-up (right) as a function of the number of processors for different problem sizes using the PCGASM preconditioner. The black lines represent efficiency benchmarks, while the various line colors and markers represent various problem sizes.

compared to the advective (CFL-A) and diffusive (CFL-D) ratios. Wall-clock time per step and respective speedup are shown in Fig. 15. These results correspond to a strong scaling performance analysis and are averaged over 10 time steps.

It is apparent that the solver demonstrates good strong scaling performance on problems from 1 M to 20 M using up to thousands of processors. The scaling behavior is close to ideal on $\mathcal{O}(100)$ processors, but a loss of efficiency is observed near $\mathcal{O}(1000)$ processors. Performance results for the largest problem (19.2 M) using 112 processors are shown for the sake of completeness, but due to memory limitations, the simulations required more nodes than all other configurations using 112 processors. Consequently, the data point is not included in the calculation of the parallel efficiency and speed-up shown.

The costs associated with each component of the preconditioner are also of interest. Table 7 provides a breakdown of the computational costs, which is representative of all the preconditioning strategies used in this study.

Preconditioning the system is by far the most expensive portion of the solution approach, making up roughly 75% of the overall cost. Within the preconditioner application, the cost associated with preconditioning the electric potential is largest, making up about half of the overall cost of the simulation. This is followed by the cost of function evaluations at 20% and then ion and electron preconditioning. As mentioned prior, the cost of accounting for the kinetics coupling across charges (i.e. the solution of 3×3 blocks along the diagonal of the block-diagonal matrix Q) makes up a very small fraction of the overall computational cost.

Table 7Breakdown of computational costs. The fractions do not vary significantly for the different inner preconditioners presented in this study.

Section	Linear system	Fraction
Preconditioning	P_n P_u P_v P_{φ} Q	12% 8% 8% 46% 2%
Func. Eval. GMRES Orthog.	-	20% 3%

9. Conclusions

A system of nonlinear partial differential equations for electrons, positive ions and negative ions, and electrostatic potential is considered to simulate streamers igniting and propagating during Nanosecond Pulsed Discharges. The plasma fluid model includes charge drift under an electric field, diffusion and chemical kinetics processes for all plasma particles, and includes physically accurate nonlinear boundary conditions. Integration of the systems of equations in time is performed with high-order time-implicit methods based on Backward Differentiation Formulas. The fully coupled, monolithic system is solved at each time step using a preconditioned Jacobian-free Newton-Krylov (JFNK) approach. We proposed a novel preconditioning strategy that makes use of linearization and operator splitting to reduce the computational cost of applying the preconditioner.

The JFNK with our novel preconditioning approach is demonstrated by simulating two discharge configurations that feature streamer ignition and propagation: between parallel plates, and across a gap between parabolic pins. The performance of the preconditioner is then assessed through the use of relevant metrics. The parallel plates configuration is a best-case scenario whereby the effect of boundary conditions and electrode sheaths is absent. Under these conditions we observe excellent performance results with respect to the number of GMRES and Newton iterations with time step sizes up to 30 ps, and the effect of reusing matrix factorizations was also explored. The gap discharge test case provides a more practical and realistic test for the formation and propagation of streamers. For this configuration, similar time step sizes were observed, but the preconditioner was less effective in lowering the number of GMRES compared to the parallel plates case due to nonlinear boundary conditions at the anode surface, which support the formation of a plasma sheath, i.e. a region of very steep gradients in space charge.

The JFNK method was successful in overcoming typical time step constraints imposed by electric drift, diffusive, and dielectric processes at a reasonable cost. The results are encouraging for future development of robust and efficient solvers for plasma discharges. The use of ILU/LU decompositions for linear systems associated with the application of the preconditioner for ions and electrostatic potential can be replaced with more scalable and efficient approaches, which provide obvious advantages for plasma kinetics mechanisms consisting of a large number of ions.

Numerical experiments with homogeneous Neumann boundary conditions for all charges at the anode surface showed nearly identical streamer ignition and propagation with a sixfold decrease in overall wall-clock time. The results confirm challenges associated with the use of nonlinear numerical boundary conditions in the presence of large number densities and elevated electric field strengths near the anode. The excellent performance observed with homogeneous Neumann conditions provides best-case scenario performance metrics for future improvements to the preconditioning approach specific to the equations on the anode boundary.

Some commentary is also provided with respect to the current curvilinear mesh generation approach without source terms to control clustering of points. New techniques have been developed since the classic method [59,60] used here that allow control point placement tightly. There is some indication that the use of these techniques to cluster the points near electrode surfaces could improve the rate of convergence of the iterative solver without increasing problem size.

Under the proposed preconditioning framework, the cost of the preconditioner, which accounts for most of the overall cost, is expected to scale proportionally to the number of ion species included. With a slight modification of the framework, and assuming that multiple ion species share similar transport properties, such as electric mobility, the same matrix factors can be used to precondition more than one ion species. This modification would allow to include more ion species at a limited cost.

Additional venues for future work include the extension to more detailed plasma chemistry, incorporating photoionization, coupling to a circuit model [61], and the extension of the approach to spatial discretizations that feature adaptive mesh refinement.

CRediT authorship contribution statement

Alfredo Duarte Gomez: Data curation, Formal analysis, Software, Validation, Visualization, Writing – original draft. **Nicholas Deak:** Methodology, Supervision, Writing – review & editing. **Fabrizio Bisetti:** Conceptualization, Project administration, Supervision, Writing – review & editing.

Declaration of competing interest

The authors declare that they have no known competing financial interests or personal relationships that could have appeared to influence the work reported in this paper.

Data availability

Data will be made available on request.

Acknowledgements

This research was supported by NSF grant #1903775 and DOE contract DE-EE0008874, along with computing resources provided by the Texas Advanced Computing Center (TACC) and the National Renewable Energy Laboratory (NREL).

Appendix A. Electron impact ionization rates

Electron impact ionization rates can be pre-computed using the Boltzmann solver BOLSIG+ [36] and cross section data for N₂ and O₂. The ionization rate is a function of the mean electron energy. Under the local field approximation (LFA), and constant background gas temperature and pressure, the ionization rate \tilde{r}_i is a function of the reduced electric field $\tilde{\theta}/\tilde{N}_B$. In this work, the functional form given in the Appendix of Ref. [31] is used. In this case, the reduced ionization rate coefficient \tilde{k}_i is a product of the magnitude of the drift velocity of electrons and the reduced ionization coefficient $\tilde{k}_i = |\tilde{W}_e|\tilde{\alpha}/\tilde{N}_B$.

$$\tilde{\alpha}/\tilde{N}_B = 2.0 \times 10^{-16} \exp\left(-7.248 \times 10^{-15}/(\tilde{\theta}/\tilde{N}_B)\right) \text{ cm}^2$$

$$\tilde{\theta}/\tilde{N}_B > 1.5 \times 10^{-15} \text{ V cm}^2,$$
(A.1)

$$= 6.619 \times 10^{-17} \exp\left(-5.593 \times 10^{-15} / (\tilde{\theta}/\tilde{N}_B)\right) \text{ cm}^2$$

$$\tilde{\theta}/\tilde{N}_B < 1.5 \times 10^{-15} \text{ V cm}^2,$$
(A.2)

and the magnitude of the drift velocity of electrons is given by

$$|\tilde{W}_e| = 7.4 \times 10^{21} (\tilde{\theta}/\tilde{N}_B) + 7.1 \times 10^6 \text{ cm s}^{-1}$$

$$\tilde{\theta}/\tilde{N}_B > 2.0 \times 10^{-15} \text{ V cm}^2,$$
(A.3)

$$|\tilde{W}_e| = 1.03 \times 10^{22} (\tilde{\theta}/\tilde{N}_B) + 1.3 \times 10^6 \text{ cm s}^{-1}$$

$$10^{-16} \le \tilde{\theta}/\tilde{N}_B \le 2.0 \times 10^{-15} \text{ V cm}^2,$$
(A.4)

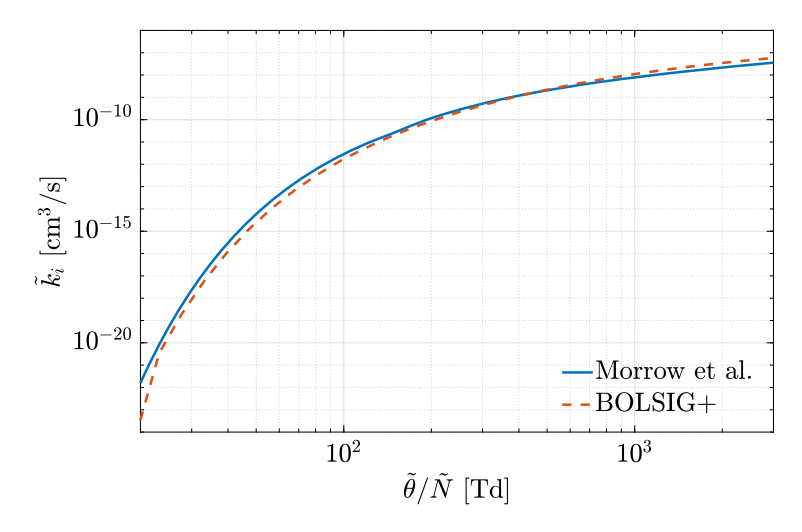


Fig. A.16. Ionization rate \tilde{k}_i for air. Comparison between the functional form in Ref. [31] and that computed using BOLSIG+.

$$|\tilde{W}_e| = 7.2973 \times 10^{21} (\tilde{\theta}/\tilde{N}_B) + 1.63 \times 10^6 \text{ cm s}^{-1}$$
 (A.5)

$$2.6 \times 10^{-17} \le \tilde{\theta} / \tilde{N}_B \le 10^{-16} \,\mathrm{V \, cm}^2$$

$$|\tilde{W}_e| = 6.87 \times 10^{22} (\tilde{\theta}/\tilde{N}_B) + 3.38 \times 10^4 \text{ cm s}^{-1}$$
 (A.6)

$$\tilde{\theta}/\tilde{N}_B < 2.6 \times 10^{-17} \,\mathrm{V \, cm}^2.$$
 (A.7)

A comparison for \tilde{k}_i and the BOLSIG+ rates using the Morgan cross section database [37] is shown in Fig. A.16, which shows good agreement for the range of reduced electric field magnitudes observed in the two test configurations.

Appendix B. Electron detachment

The dimensional detachment rate constant is

$$\tilde{k}_d = 10^{f(\tilde{T}_B)} + 10^{g(\tilde{\theta}/\tilde{N}_B)} [\text{cm}^3/\text{s}],$$

where the temperature dependent component $f(\tilde{T}_B)$ is a second order polynomial and the component that depends on the reduced electric field $g(\tilde{\theta}/\tilde{N})$, is a fourth order polynomial. The expressions of the functional fits are (temperature \tilde{T}_B is in Kelvin and the reduced electric field $\tilde{\theta}/\tilde{N}_B$ is in Townsend),

$$\begin{split} f(\tilde{T}_B) &= c_{d1} \tilde{T}_B^2 + c_{d2} \tilde{T}_B + c_{d3}, \\ g(\tilde{\theta}/\tilde{N}_B) &= c_{d4} (\tilde{\theta}/\tilde{N}_B)^4 + c_{d5} (\tilde{\theta}/\tilde{N}_B)^3 + c_{d6} (\tilde{\theta}/\tilde{N}_B)^2 + c_{d7} (\tilde{\theta}/\tilde{N}_B) + c_{d8}, \\ c_{d1} &= -2.026 \times 10^{-5}, \\ c_{d2} &= 3.062 \times 10^{-2}, \\ c_{d3} &= -2.470 \times 10^1, \\ c_{d4} &= -1.319 \times 10^{-9}, \\ c_{d5} &= 1.305 \times 10^{-6}, \\ c_{d6} &= -4.818 \times 10^{-4}, \\ c_{d7} &= 8.344 \times 10^{-2}, \\ c_{d8} &= -1.653 \times 10^1. \end{split}$$

The polynomials were fit to the data in Fig. 2 in Ref. [34] and Fig. 11 in Ref. [40].

Appendix C. Curvilinear meshes

The generation of a curvilinear mesh uses the approach in Ref. [58], which consists of solving a system of elliptic equations of the form

$$\nabla^2 \xi = P(\xi),$$
$$\nabla^2 \eta = O(\eta).$$

where $P(\xi)$ and $Q(\eta)$ are continuously differentiable functions that control the spacing of the grid lines. We limit ourselves to the case in which $P(\xi)$ and $Q(\eta)$ are equal to 0. Changing the dependent and independent variables we obtain the system of equations

$$\alpha r_{\xi\xi} - 2\beta r_{\xi\eta} + \gamma r_{\eta\eta} = 0,$$

$$\alpha z_{\xi\xi} - 2\beta z_{\xi\eta} + \gamma z_{\eta\eta} = 0,$$

subject to the Dirichlet boundary conditions in Eqs. (112) to (119) presented in Section 7.3 and

$$\alpha = r_{\eta}^2 + z_{\eta}^2,$$

$$\gamma = r_{\xi}^2 + z_{\xi}^2,$$

$$\beta = r_{\eta}r_{\xi} + z_{\eta}z_{\xi}.$$

We require expressions for the operators that appear in the PDEs, namely $\theta \cdot \nabla$ and the Laplacian operator Δ . A cylindrical coordinate system is considered where r is the radial distance, ψ is the azimuthal angle about the longitudinal axis, and z is the axial coordinate along the longitudinal axis. We define the transformation $\Pi : (r, \psi, z) \longrightarrow (\xi, \alpha, \eta)$

$$\xi = \xi(r, z)$$
,

$$\psi = \alpha$$
,

$$\eta = \eta(r, z)$$
.

And its inverse $\Pi^{-1}: (\xi, \alpha, \eta) \longrightarrow (r, \psi, z)$

$$r = r(\xi, \eta),$$

$$\alpha = \psi$$
,

$$z = z(\xi, \eta)$$
.

The determinant of the Jacobian matrix transformation is

$$J = \frac{\partial \xi}{\partial r} \frac{\partial \eta}{\partial z} - \frac{\partial \xi}{\partial z} \frac{\partial \eta}{\partial r},$$

and the determinant of the inverse transformation

$$J^{-1} = \frac{\partial r}{\partial \xi} \frac{\partial z}{\partial \eta} - \frac{\partial r}{\partial \eta} \frac{\partial z}{\partial \xi}.$$

For position vector \mathbf{x} , the local (unnormalized) tangent basis vectors \mathbf{e}_{ξ} , \mathbf{e}_{α} , \mathbf{e}_{η} in cylindrical components read

$$\mathbf{e}_{\xi} = \frac{\partial r}{\partial \xi} \hat{\mathbf{e}}_r + \frac{\partial z}{\partial \xi} \hat{\mathbf{e}}_z,$$

$$\mathbf{e}_{\alpha} = r\hat{\mathbf{e}}_{\psi}$$

$$\mathbf{e}_{\eta} = \frac{\partial r}{\partial \eta} \hat{\mathbf{e}}_r + \frac{\partial z}{\partial \eta} \hat{\mathbf{e}}_z,$$

where $\hat{\bf e}_{\bf r}$, $\hat{\bf e}_{\psi}$, and $\hat{\bf e}_{\bf z}$ are the normalized basis vectors in cylindrical coordinates. The local (unnormalized) dual basis vectors ${\bf e}^{\xi}$, ${\bf e}^{\alpha}$, ${\bf e}^{\eta}$ in cylindrical components read

$$\mathbf{e}^{\xi} = \frac{\partial \xi}{\partial r} \hat{\mathbf{e}}_r + \frac{\partial \xi}{\partial z} \hat{\mathbf{e}}_z,$$

$$\mathbf{e}^{\alpha} = \frac{1}{r} \hat{\mathbf{e}}_{\psi},$$

$$\mathbf{e}^{\eta} = \frac{\partial \eta}{\partial r} \hat{\mathbf{e}}_r + \frac{\partial \eta}{\partial z} \hat{\mathbf{e}}_z.$$

The elements of the inverse of the metric tensor read

$$\overline{g}^{\xi\xi} = J^2 \left[\left(\frac{\partial z}{\partial \eta} \right)^2 + \left(\frac{\partial r}{\partial \eta} \right)^2 \right],$$

$$\overline{g}^{\alpha\alpha} = 1/r^2$$
,

$$\overline{g}^{\eta\eta} = J^2 \left[\left(\frac{\partial z}{\partial \xi} \right)^2 + \left(\frac{\partial r}{\partial \xi} \right)^2 \right],$$

$$\overline{g}^{\xi\eta} = -J^2 \left[\frac{\partial z}{\partial \xi} \frac{\partial z}{\partial \eta} + \frac{\partial r}{\partial \xi} \frac{\partial r}{\partial \eta} \right],$$

$$\overline{g}^{\xi\alpha}=0$$
,

$$\overline{g}^{\alpha\eta} = 0$$
,

where the zero elements are due to the orthogonality of \mathbf{e}^{α} with both \mathbf{e}^{ξ} , and \mathbf{e}^{η} . Let us now consider the desired operators in an axisymmetric configuration. The operator $\boldsymbol{\theta} \cdot \nabla$ is computed as

$$\boldsymbol{\theta} \cdot \nabla = \theta^{\xi} \frac{\partial}{\partial \xi} + \theta^{\eta} \frac{\partial}{\partial \eta},$$

where the components of the electric field are obtained by the application of linear differential operators to the scalar field φ .

$$\theta^{\xi} = -\left(\overline{g}^{\xi\xi} \frac{\partial \varphi}{\partial \xi} + \overline{g}^{\xi\eta} \frac{\partial \varphi}{\partial \eta}\right),$$

$$\theta^{\eta} = -\left(\overline{g}^{\xi\eta} \frac{\partial \varphi}{\partial \xi} + \overline{g}^{\eta\eta} \frac{\partial \varphi}{\partial \eta}\right).$$

Similarly, the Laplacian operator reads

$$\begin{split} & \Delta = \overline{g}^{\xi\xi} \frac{\partial^2}{\partial \xi^2} + 2 \overline{g}^{\xi\eta} \frac{\partial^2}{\partial \xi \partial \eta} + \overline{g}^{\eta\eta} \frac{\partial^2}{\partial \eta^2} \\ & + \left[\frac{1}{\sigma} \frac{\partial (\sigma \overline{g}^{\xi\xi})}{\partial \xi} + \frac{1}{\sigma} \frac{\partial (\sigma \overline{g}^{\xi\eta})}{\partial \eta} \right] \frac{\partial}{\partial \xi} + \left[\frac{1}{\sigma} \frac{\partial (\sigma \overline{g}^{\xi\eta})}{\partial \xi} + \frac{1}{\sigma} \frac{\partial (\sigma \overline{g}^{\eta\eta})}{\partial \eta} \right] \frac{\partial}{\partial \eta}, \end{split}$$

where $\sigma = rJ^{-1}$. Singularities exist at the axis where r = 0, and while expressions exist in the limit of $\partial/\partial r \to 0$, in practical terms, evaluation of the Laplacian on the axis is not needed because it is replaced by homogeneous Neumann boundary condition consistent with the axisymmetric configuration.

References

- [1] N. Deak, A. Bellemans, F. Bisetti, Plasma-assisted ignition of methane/air and ethylene/air mixtures: efficiency at low and high pressures, Proc. Combust. Inst. (2020).
- [2] J.E. Foster, S. Mujovic, J. Groele, I.M. Blankson, Towards high throughput plasma based water purifiers: design considerations and the pathway towards practical application, J. Phys. D, Appl. Phys. 51 (2018) 293001.
- [3] J. Kruszelnicki, A.M. Lietz, M.J. Kushner, Atmospheric pressure plasma activation of water droplets, J. Phys. D, Appl. Phys. 52 (2019) 355207.
- [4] W. Kim, M. Godfrey Mungal, M.A. Cappelli, The role of in situ reforming in plasma enhanced ultra lean premixed methane/air flames, Combust. Flame 157 (2010) 374–383.
- [5] A.V. Nastuta, I. Topala, C. Grigoras, V. Pohoata, G. Popa, Stimulation of wound healing by helium atmospheric pressure plasma treatment, J. Phys. D, Appl. Phys. 44 (2011) 105204.
- [6] A. Kulikovsky, Two-dimensional simulation of the positive streamer in N2 between parallel-plate electrodes, J. Phys. D, Appl. Phys. 28 (1995) 2483.
- [7] S.V. Pancheshnyi, A.Y. Starikovskii, Two-dimensional numerical modelling of the cathode-directed streamer development in a long gap at high voltage, J. Phys. D, Appl. Phys. 36 (2003) 2683–2691.
- [8] S. Pancheshnyi, P. Ségur, J. Capeillère, A. Bourdon, Numerical simulation of filamentary discharges with parallel adaptive mesh refinement, J. Comput. Phys. 227 (2008) 6574–6590.
- [9] A. Villa, L. Barbieri, M. Gondola, A.R. Leon-Garzon, R. Malgesini, An implicit three-dimensional fractional step method for the simulation of the corona phenomenon, Appl. Math. Comput. 311 (2017) 85–99.
- [10] J. Teunissen, U. Ebert, Afivo: a framework for quadtree/octree AMR with shared-memory parallelization and geometric multigrid methods, Comput. Phys. Commun. 233 (2018) 156–166.
- [11] R. Marskar, An adaptive Cartesian embedded boundary approach for fluid simulations of two- and three-dimensional low temperature plasma filaments in complex geometries, J. Comput. Phys. 388 (2019) 624–654.
- [12] J. Van Dijk, K. Peerenboom, M. Jimenez, D. Mihailova, J. Van der Mullen, The plasma modelling toolkit Plasimo, J. Phys. D, Appl. Phys. 42 (2009) 194012.
- [13] D. Breden, L.L. Raja, C.A. Idicheria, P.M. Najt, S. Mahadevan, A numerical study of high-pressure non-equilibrium streamers for combustion ignition application, J. Appl. Phys. 114 (2013) 083302.
- [14] R.N. Franklin, The plasma-sheath boundary region, J. Phys. D, Appl. Phys. 36 (2003) R309-R320.
- [15] M. Niknezhad, O. Chanrion, C. Kahn, J. Holbøll, T. Neubert, A three-dimensional model of streamer discharges in unsteady airflow, Plasma Sources Sci. Technol. 30 (2021) 045012.
- [16] B. Lin, C. Zhuang, Z. Cai, R. Zeng, W. Bao, An efficient and accurate MPI-based parallel simulator for streamer discharges in three dimensions, J. Comput. Phys. 401 (2020) 109026.
- [17] R. Frascella, J. Velasco, R. Albarracín, V. Antonio Primo, 2018 IEEE 2nd International Conference on Dielectrics (ICD), 2018, pp. 1-4.
- [18] T.N. Tran, I.O. Golosnoy, P.L. Lewin, G.E. Georghiou, Numerical modelling of negative discharges in air with experimental validation, J. Phys. D, Appl. Phys. 44 (2010) 015203.
- [19] D. Knoll, D. Keyes, Jacobian-free Newton-Krylov methods: a survey of approaches and applications, J. Comput. Phys. 193 (2004) 357-397.
- [20] J. Reisner, A. Wyszogrodzki, V. Mousseau, D. Knoll, An efficient physics-based preconditioner for the fully implicit solution of small-scale thermally driven atmospheric flows, J. Comput. Phys. 189 (2003) 30–44.
- [21] H.K. Park, R.R. Nourgaliev, R.C. Martineau, D.A. Knoll, On physics-based preconditioning of the Navier-Stokes equations, J. Comput. Phys. 228 (2009) 9131–9146.
- [22] Q. Tang, L. Chacón, T.V. Kolev, J.N. Shadid, X.Z. Tang, An adaptive scalable fully implicit algorithm based on stabilized finite element for reduced visco-resistive MHD, J. Comput. Phys. 454 (2022).
- [23] V. Mousseau, D. Knoll, W. Rider, Physics-based preconditioning and the Newton-Krylov method for non-equilibrium radiation diffusion, J. Comput. Phys. 160 (2000) 743–765.
- [24] D.A. Knoll, W.B. VanderHeyden, V.A. Mousseau, D.B. Kothe, On preconditioning Newton-Krylov methods in solidifying flow applications, SIAM J. Sci. Comput. 23 (2001) 381–397.
- [25] G. Hammond, A. Valocchi, P. Lichtner, Application of Jacobian-free Newton-Krylov with physics-based preconditioning to biogeochemical transport, Adv. Water Resour. 28 (2005) 359–376.

- [26] B. Weston, R. Nourgaliev, J.-P. Delplanque, A.T. Barker, Preconditioning a Newton-Krylov solver for all-speed melt pool flow physics, J. Comput. Phys. 397 (2019) 108847.
- [27] B. Aksoylu, H. Klie, A family of physics-based preconditioners for solving elliptic equations on highly heterogeneous media, Appl. Numer. Math. 59 (2009) 1159–1186.
- [28] G. Chen, L. Chacón, C. Leibs, D. Knoll, W. Taitano, Fluid preconditioning for Newton–Krylov-based, fully implicit, electrostatic particle-in-cell simulations, J. Comput. Phys. 258 (2014) 555–567.
- [29] G.V. Naidis, Effects of nonlocality on the dynamics of streamers in positive corona discharges, Tech. Phys. Lett. 23 (1997) 493.
- [30] N. Liu, V.P. Pasko, Effects of photoionization on propagation and branching of positive and negative streamers in sprites, J. Geophys. Res. Space Phys. 109 (2004).
- [31] R. Morrow, J.J. Lowke, Streamer propagation in air, J. Phys. D, Appl. Phys. 30 (1997) 614-627.
- [32] B. Bagheri, J. Teunissen, U. Ebert, M.M. Becker, S. Chen, O. Ducasse, O. Eichwald, D. Loffhagen, A. Luque, D. Mihailova, J.M. Plewa, J. van Dijk, M. Yousfi, Comparison of six simulation codes for positive streamers in air, Plasma Sources Sci. Technol. 27 (2018) 095002.
- [33] I.A. Kossyi, A.Y. Kostinsky, A.A. Matveyev, V.P. Silakov, Kinetic scheme of the non-equilibrium discharge in nitrogen-oxygen mixtures, Plasma Sources Sci. Technol. 1 (1992) 207.
- [34] N.L. Aleksandrov, E.M. Anokhin, Electron detachment from O2 ions in oxygen: the effect of vibrational excitation and the effect of electric field, J. Phys. B, At. Mol. Opt. Phys. 44 (2011) 115202.
- [35] A. Ponomarev, N. Aleksandrov, Monte Carlo simulation of electron detachment properties for ions in oxygen and oxygen: nitrogen mixtures, Plasma Sources Sci. Technol. 24 (2015) 035001.
- [36] G. Hagelaar, L. Pitchford, Solving the Boltzmann equation to obtain electron transport coefficients and rate coefficients for fluid models, Plasma Sources Sci. Technol. 14 (2005) 722.
- [37] S. Pancheshnyi, S. Biagi, M. Bordage, G. Hagelaar, W. Morgan, A. Phelps, L. Pitchford, The LXCat project: electron scattering cross sections and swarm parameters for low temperature plasma modeling, Chem. Phys. 398 (2012) 148–153.
- [38] M.F. L'Annunziata, Handbook of Radioactivity Analysis, 3rd edition, Elsevier Science & Technology, San Diego, 2012.
- [39] S. Pancheshnyi, Role of electronegative gas admixtures in streamer start, propagation and branching phenomena, Plasma Sources Sci. Technol. 14 (2005) 645.
- [40] A.A. Ponomarev, N.L. Aleksandrov, Monte Carlo simulation of electron detachment properties for O2- ions in oxygen and oxygen: nitrogen mixtures, Plasma Sources Sci. Technol. 24 (2015) 035001.
- [41] V. Gorin, A. Kudryavtsev, J. Yao, C. Yuan, Z. Zhou, Boundary conditions for drift-diffusion equations in gas-discharge plasmas, Phys. Plasmas 27 (2020) 013505.
- [42] E. Hairer, G. Wanner, Solving Ordinary Differential Equations II: Stiff and Differential-Algebraic Problems, Springer, Berlin, 1996.
- [43] M. Calvo, J.I. Montijano, L. Rández, Ao-stability of variable stepsize BDF methods, J. Comput. Appl. Math. 45 (1993) 29-39.
- [44] M. Calvo, F. Lisbona, J. Montijano, On the stability of variable-stepsize Nordsieck BDF methods, SIAM J. Numer. Anal. 24 (1987) 844-854.
- [45] A.C. Hindmarsh, P.N. Brown, K.E. Grant, S.L. Lee, R. Serban, D.E. Shumaker, C.S. Woodward, SUNDIALS: suite of nonlinear and differential/algebraic equation solvers, ACM Trans. Math. Softw. 31 (2005) 363–396.
- [46] Y. Saad, Iterative Methods for Sparse Linear Systems, SIAM, Philadelphia, USA, 2003.
- [47] S. Balay, S. Abhyankar, M.F. Adams, S. Benson, J. Brown, P. Brune, K. Buschelman, E. Constantinescu, L. Dalcin, A. Dener, V. Eijkhout, W.D. Gropp, V. Hapla, T. Isaac, P. Jolivet, D. Karpeev, D. Kaushik, M.G. Knepley, F. Kong, S. Kruger, D.A. May, L.C. McInnes, R.T. Mills, L. Mitchell, T. Munson, J.E. Roman, K. Rupp, P. Sanan, J. Sarich, B.F. Smith, S. Zampini, H. Zhang, H. Zhang, J. Zhang, PETSc/TAO Users Manual, Technical Report ANL-21/39 Revision 3.15, Argonne National Laboratory, 2022.
- [48] S. Abhyankar, J. Brown, E.M. Constantinescu, D. Ghosh, B.F. Smith, H. Zhang, PETSc/TS: a Modern Scalable ODE/DAE Solver Library, Technical Report, 2018.
- [49] R.D. Falgout, U.M. Yang, hypre: A Library of High Performance Preconditioners, Springer Berlin Heidelberg, Berlin, Heidelberg, 2002, pp. 632-641.
- [50] P. Amestoy, I.S. Duff, J. Koster, J.-Y. L'Excellent, A fully asynchronous multifrontal solver using distributed dynamic scheduling, SIAM J. Matrix Anal. Appl. 23 (2001) 15–41.
- [51] P. Amestoy, A. Buttari, J.-Y. L'Excellent, T. Mary, Performance and scalability of the block low-rank multifrontal factorization on multicore architectures, ACM Trans. Math. Softw. 45 (2019) 2.
- [52] G.E. Georghiou, R. Morrow, A.C. Metaxas, The effect of photoemission on the streamer development and propagation in short uniform gaps, J. Phys. D, Appl. Phys. 34 (2000) 200–208.
- [53] C. Zhuang, R. Zeng, B. Zhang, J. He, A WENO scheme for simulating streamer discharge with photoionizations, IEEE Trans. Magn. 50 (2014) 325-328.
- [54] F. Tholin, A. Bourdon, Influence of temperature on the glow regime of a discharge in air at atmospheric pressure between two point electrodes, J. Phys. D, Appl. Phys. 44 (2011).
- [55] F. Tholin, A. Bourdon, Simulation of the stable 'quasi-periodic' glow regime of a nanosecond repetitively pulsed discharge in air at atmospheric pressure, Plasma Sources Sci. Technol. 22 (2013) 045014.
- [56] A. Zhang, R. Scarcelli, T. Wallner, D. Breden, A. Karpatne, L.L. Raja, I. Ekoto, B. Wolk, Numerical investigation of nanosecond pulsed discharge in air at above-atmospheric pressures, J. Phys. D, Appl. Phys. 51 (2018).
- [57] J.-M. Plewa, O. Eichwald, O. Ducasse, P. Dessante, C. Jacobs, N. Renon, M. Yousfi, 3D streamers simulation in a pin to plane configuration using massively parallel computing, J. Phys. D, Appl. Phys. 51 (2018) 095206.
- [58] J.F. Thompson, F.C. Thames, C. Mastin, Automatic numerical generation of body-fitted curvilinear coordinate system for field containing any number of arbitrary two-dimensional bodies, J. Comput. Phys. 15 (1974) 299–319.
- [59] L. Eça, 2D orthogonal grid generation with boundary point distribution control, J. Comput. Phys. 125 (1996) 440-453.
- [60] V. Akcelik, B. Jaramaz, O. Ghattas, Nearly orthogonal two-dimensional grid generation with aspect ratio control, J. Comput. Phys. 171 (2001) 805-821.
- [61] V. Gururajan, R. Scarcelli, A nanosecond pulsed discharge circuit model for engine applications, J. Phys. D, Appl. Phys. 55 (2022) 155205.